Temperature-dependence of NbN photon detector behavior

Marc van Kralingen

May 29, 2012

Bachelor Thesis

Supervised by:
Jelmer Renema
Martin van Exter

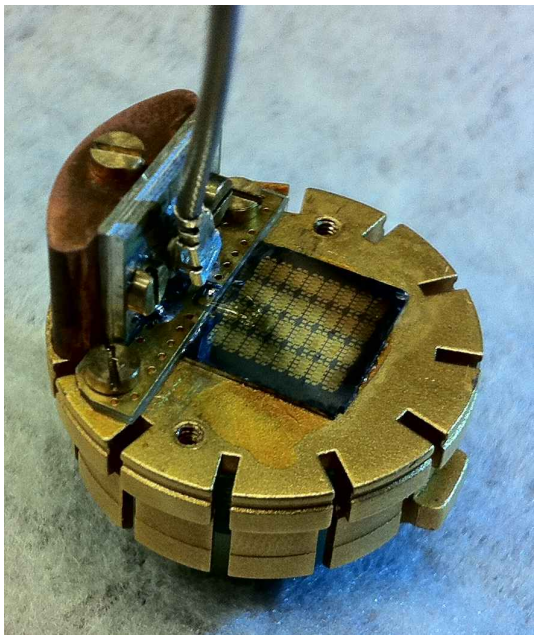

Quantum Optics group
Leiden University

Temperature-dependence of NbN photon detector behavior

Marc van Kralingen

Bachelor Thesis

Contents

1 Introduction

Superconducting nanowire single-photon detectors are promising devices because these detectors combine a high detection efficiency (highest published value: 47.7% at 1550 nm [1] and a short reset time (few ns) [2]). High-speed photodetectors have many applications. The two most important branches are quantum communication [3] and free-space optical communication [4]. Since the pioneering research on superconducting nanowires [5] thin-film superconductors have been a matter of interest for both experimental and theoretical research ([6],[7],[8] and the citations therein).

A schematic overview of the detection mechanism is given in fig. 1.

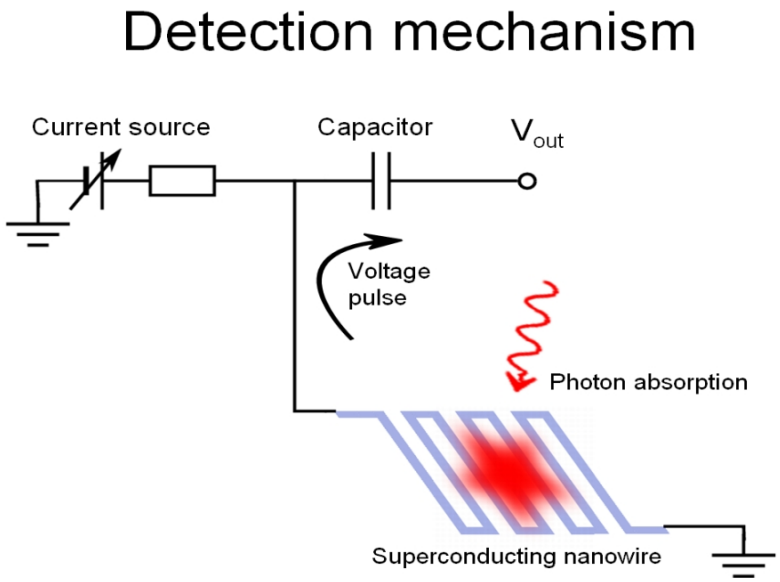

Figure 1: The detection mechanism for superconducting nanowire single-photon detectors in general. The superconducting nanowire in meander form is biased by a current source. The superconductivity is disturbed when the detector absorbs a photon. The resulting voltage pulse can be measured.

My bachelor project involved the construction of a setup for Niobium-Nitride (NbN) photodetectors and the characterization of our detector. This research forms a basis for the future research on photon detection efficiency. This thesis consists of an overview of the available literature, an extensive description of the setup and the presentation of our characterization measurements. It is organized as follows: In chapter 2 we describe firstly the transition of superconductors to the normal state and the different experi-

mental definitions for this transition. Secondly we explain the single photon detection mechanism in general and the formation of self-spreading hotspots within a superconducting device at high bias current levels. Chapter 3 contains a description of the experimental setup, comprising the detector geometry, the surrounding equipment (the temperature regulation, the optical access, the bias current source) and the voltage pulse measurement system. The measurement results are divided into two chapters: Chapter 4 on the critical current behavior and chapter 5 on the self-heating hotspot measurements. Both chapters include a discussion of the measurement results.

2 Theory

In this chapter we give a brief theoretical background for superconducting nanowire single-photon detectors in general and our measurements in particular. This theory is divided into four parts:

1. The most important phenomena in the transition of thin-film superconductors to the normal state.

2. A literature study on the experimental determination of the critical current.

3. The disturbance of superconductivity as basis for the detection mechanism.

4. Stabilization of resistive parts within a superconducting nanowire.

2.1 Two-dimensional superconductivity

In the superconducting state the resistivity is generally equal to zero. The most used description is given by the Bardeen-Cooper-Schrieffer (BCS) theory. In the BCS theory electrons close to the Fermi-level pair into Cooper pairs, so that the energy is lowered leaving an energy gap between the paired and unpaired states. At a certain current density level, the critical current, the kinetic energy of the Cooper pairs becomes larger then the energy gap and the material becomes resistive. The value of the critical current level depends on the temperature. The critical current is lower at higher temperatures.

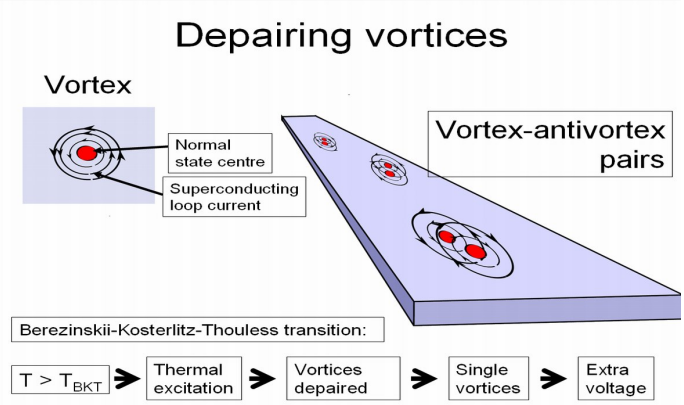

Figure 2: Schematic overview of the Berezinskii-Kosterlitz-Thouless transition.

For further analysis of the temperature-dependence of the critical current, we have to mention the effect of vortices in two-dimensional superconductors, described mathematically in detail by J. E. Mooij.[9] (The two-dimensionality of thin-film nanowires is demonstrated by Aslamazov *et al.*[10]) A vortex is a small area in the normal state with a superconducting loop current around it. At low temperatures vortices occur mostly in pairs of clockwise and counterclockwise vortices: Vortex-antivortex pairs. At higher temperature vortex-antivortex pairs break-up by thermal excitation. Single vortices move through the material and cause an extra voltage over the device. This process also occurs close to the critical current. Therefore, in practise, the extra voltage due to moving single vortices is visible in the lowering of the steepness of the voltage transition to the normal state.

The steepness transition due to the vortex-antivortex binding is called the Berezinskii-Kosterlitz-Thouless (BKT) transition [11], see fig. 2. The transition is specified by the BKT-temperature T_{BKT}. Approximately the voltage behavior in the intermediate range between the superconducting state and the normal state can be described by

$$V = I^{\alpha(T)}. \tag{1}$$

where $\alpha(T) = 2(\mathrm{T}_{BKT}/\mathrm{T}) + 1$ [12], such that $\alpha(T) = 3$ at $\mathrm{T} = \mathrm{T}_{BKT}$ (p. 350-352 of ref. [9]). The application of this definition is described in detail by Eley *et al.*[12]

The temperature dependence of the critical current suggested by Bardeen is:[13]

$$I_C(T) = C\left(1 - \frac{T^2}{T_C^2}\right)^{\frac{3}{2}}, \tag{2}$$

where T_C is the critical temperature. The simplified definition for the critical temperature is: the temperature where the critical current is equal to zero. The detailed definition is described by Fiory *et al.*[14] However, the experimental critical current values show a deviation above a certain temperature due to the BKT-transition (section 4.3). Notice that, according to the Ginzburg-Landau theory, the I_C converges to

$$I_C(T) \sim \left(1 - \frac{T}{T_C}\right)^{\frac{3}{2}}, \tag{3}$$

for $\mathrm{T} \approx \mathrm{T}_C$ (p. 124 of ref. [15]).

2.2 Methods to measure the critical current

The value of the critical current of the whole device depends on the experimental definition that one chooses, because of several reasons:

- The voltage near the critical current is induced by different mechanisms (phase-slips, hotspots). Therefore the critical current behavior cannot be described by one theory alone.

- The transition doesn't happen at a specific current level, because the device can be partially in the normal state and partially in the superconducting state (vortices, hotspots).

- The transition is influenced by accidental excitations.

- Insofar there is a intrinsic critical current of the material, we must still take into account that the cross-sectional area of the nanowire is not constant.

There are several experimental definitions for the critical current:

1. A specified voltage can be defined as criterion. The intersection point of the I-V curve and this criterion defines the critical current. This procedure is described on p. 396-399 of ref. [16].

2. A specified resistance can be defined as criterion. The intersection point of the I-V curve and the $R = \frac{V}{I}$ criterion defines the critical current. This procedure is described on p. 399-400 of ref. [16].

3. The critical current can be defined by the intersection with the I-axis of the slope to the I-V curve at a specified voltage criterion. This procedure is described on p. 400-402 of ref. [16].

4. The maximum in the second derivative to the I-V curve can be used as definition for the critical current. This procedure is described by Hofherr *et al.* (p. 4 of ref. [7]).

2.3 Detection mechanism

This section contains a microscopic description of the mechanics by which a single absorbed photon can result in a measurable disturbance of the superconductivity.

When a photon is absorbed by a Cooper pair, the Cooper pair first breaks up in highly excited quasiparticles: fast photoelectrons. In the downconversion a mixed distribution of interacting quasiparticles and phonons is formed. The subsequent operating stage is described by Kozorezov *et al.*: "*(...) the mixed distribution of quasiparticles and phonons, which remains strongly nonequilibrium, evolves to a quasiparticle distribution centered at the*

superconducting edge. At the same time phonons may be lost from the superconducting film into the substrate or downconverted in amorphous cap layers. This third stage the system may be regarded as the operational stage of the process. It lasts much longer than the complete duration of all the preceding cascade stages which do not last more than few nanoseconds for a Nb- or Ta-based superconducting tunnel junction. During the third stage the nonequilibrium quasiparticles can also take part in various transport processes; they may diffuse, tunnel, recombine, be trapped and detrapped, cooled, or heated. It is essentially this stage that determines the form of the superconducting tunnel junction output. The most commonly used approach to modelling the operational stage is via the Rothwarf-Taylor equations.[17][18][19]" (p. 1 of ref. [6]) The different stages in this downconversion and the different opinions about the energy levels during the downconversion are further discussed by Kozorezov *et al.*[6][20]

According to the commonly accepted description, the bias current induces disturbance of the superconductivity in a part of the nanowire: a 'hotspot' is formed.[21] The velocity of the residual Cooper pairs must increase to maintain the bias current. The Cooper pairs break up when the kinetic energy becomes larger then the bandgap energy. In this way, the bias current can cause a disturbance of the superconductivity in the whole nanowire. This hotspot model satisfies for detection in the UV and visible range. The detection mechanism for higher wavelengths (near-infrared) is more complicated; it has been extensively studied by Hofherr *et al.*[7]

Notice that in practice the induced bias current is not equal to the bias current level in de device during the disturbance of the superconductivity, because the cabling to the device behaves like a capacitor at high frequencies.

2.4 Self-heating hotspot stabilization

This section contains the description of three topics: 1) The importance of the geometry of the detector for the detection efficiency, 2) hotspot-expansion induced by Joule heating and 3) the investigation of the detector geometry by stabilizing hotspots.

The geometry of the thin-film nanowires influences the detection efficiency in two ways: 1) The width variation restricts the bias current level and 2) the thermal contact between the nanowire and its environment influences the reset time after an photon absorption:

1. When the bias current density level is locally close to the local critical current density, the local photon detection efficiency is high. The width of superconducting nanowires is typically not constant. The

narrow parts are called constrictions. The smallest constriction determines the maximum bias current level for the whole device. Therefore constrictions form a limit for the detection efficiency (investigated by Kerman *et al.*[22]).

2. The superconductivity can be recovered after a detection event when the phonons leak to the substrate and the resist, as described in section 2.3. Therefore the reset time is influenced by the thermal contact between the nanowire and its environment: the substrate and the resist.

When the critical current is exceeded a part of the device becomes resistive. The local temperature of the nanowire is determined by the equilibrium between the Joule heating produced by the hotspot and the heat flow away from the nanowire. The hotspot can cause expansion of the area in the normal state by itself, because the critical current becomes lower when the temperature increases. Hotspot-expansion, their theoretical treatment, hysteresis and the relation between hotspots and phase-slips are described extensively by Skocpol *et al.*[5] The stabilization of hotspots is described in literature for NbN microbridges.[24][25] Expansion through an large part of the detector is called 'thermal runaway' by experimentalists (p. 312 of ref. [16]). Kerman *et al.* have given an expression for the velocity of the expansion.[23] Notice that these kinds of hotspots are induced by a stable and measured bias current, in contrast with the hotspots described in section 2.3.

The shifting of the boundary between the superconducting and normal parts in the device can be investigated by measuring the voltage over the detector relative to an increasing or decreasing bias current:

- When the bias current increases slowly in small steps the critical current density is first exceeded in the smallest part of the nanowire. The expansion of the hotspot depends on the electrical circuit in the first place, because the local power density depends on the behavior of the bias current. When the system is voltage-biased, the bias current will decrease when the total resistance increase. In a current-biased system, the bias current will not decrease. The expansion will thus be larger in a current-biased system than in a voltage-biased system.

- Decreasing the bias current slowly results in a totally different behavior. Parts of the detector in the normal state will remain in the normal state at a lower bias current, because the Joule heating lowers the critical current locally. This results in a 'hysteresis'-effect. The widest parts of the detector will become superconducting first. The lowering of the temperature due to the transition to the superconducting state can cause expansion of the superconducting area. The increase of the

current when the resistance decreases restricts the expansion of the superconducting state area in case of a voltage-biased system.

The results of these procedures contain information about the constrictions of the nanowire and the local thermal contact between the nanowire and its environment. Our research on hotspot-stabilization has been focussed on the investigation of the constrictions in the nanowire.

3 Experimental setup

In this chapter the set-up is discussed in detail. The following parameters for the detector must be tunable:

- The temperature (down to $\sim$ 5K).
- Laser beam (tunable in direction and in intensity).
- The bias current (range: $\sim \pm 8\mu$A).

The first topics in this chapter are the geometry and properties of the detector. Secondly, the insert, sampleholder and cryostat will be discussed. The third section gives information about the laser beam alignment. In the last section the electronic circuit is described in detail.

3.1 Detector

The detector consists of a thin nanowire, which can be connected to an electric circuit (see section 3.4). The material of the nanowire is Niobium Nitride (NbN). It is produced in a meander form (see figures 3 and 4). The fill factor of the total active area (5x5 μm^2) is approximately 40%. The total length of the nanowire is approximately 0.1 mm. Notice that the width of the wire is not constant, because the wire is wider at the connecting corners and because of the imperfections in the production process (see section 5). The wire is wider at the edges to minimize 'current crowding' due to the kinetic inductance.[26] Both ends of the nanowire are connected to signal pads, which are large enough for wirebonding ($\sim$ 300 μm).

The thermal contact between the NbN nanowire and its environment, the substrate and the resist, may be variable.

The device is produced by D. Sahin, TU/e, by the techniques of Reactive-Ion Etching (RIE) and Electron Beam Lithography (EBL) [27]. The detector is produced on a substrate of Gallium Arsenide (GaAs) and is covered by a resist of Hydrogen Silsesquioxane (HSQ). The thickness of the resist is approximately 180 nm. It is placed on a chip, which contains 208 detectors in total.[28]

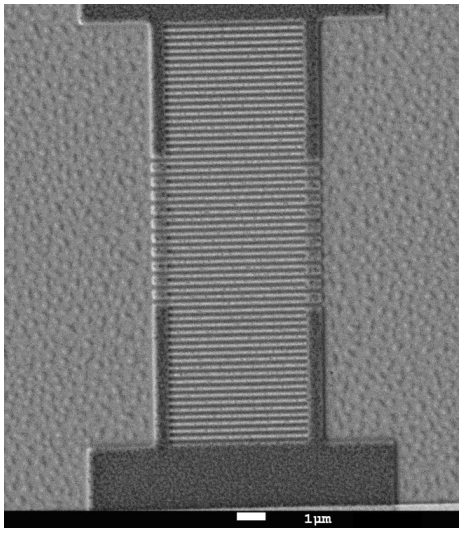

Figure 3: A Scanning Electron Microscope (SEM) picture of an SSPD nominally identical to the one used in our experiments. The picture is made by D. Sahin, TU/e. The light part of the picture is the GaAs substrate, the dark part in the middle is the NbN film. The thickness of the film is 5 ± 0.1 nm. The horizontal lines in the middle are the NbN nanowires, the width of the wires is 100 ± 5 nm with a spacing of 150 ± 5 nm. The upper and lower part are not active; the central square is the active area. A meander wire is formed by etching the even connections at the left side and the odd connections at the right side between the wires. The resulting nanowire consists of 21 branches. The size of the active area is 5x5 μm^2. Notice that the long horizontal parts of the resulting nanowire are narrower than the connecting corners. Fig. 4 is a more detailed picture of the active part of a device.

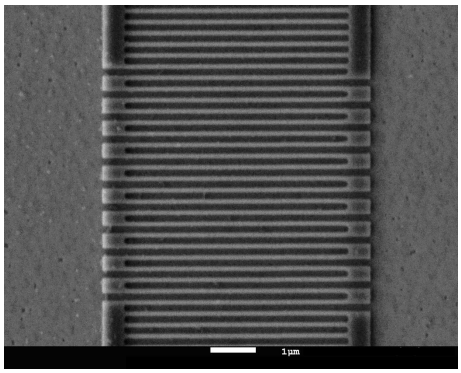

Figure 4: A detailed SEM picture of a detector nominally identical to the one used in our experiments. The picture is made by D. Sahin, TU/e. This detector was fabricated on the same sample as our detector. The 21 branches of the nanowire are clearly visible.

3.2 Temperature regulation

The detector is placed on an insert which can be placed in a cryostat. This section contains three subjects: The construction of the insert, the construction of the cryostat and the heat flow calculation.

3.2.1 Construction insert

The insert holds the detector, the electronic cabling and the laser fiber. An overview of the insert is given in fig. 5. The sample chamber is sealed between the cryostat and the insert by a KF blank flange and a centering ring with an o-ring around it (p. 30 of ref. [29]).

The sample with the detector is placed on a puck. The puck is described in the PPMS manual as: "*(...)constructed of oxygen-free high-conductivity copper that maintains high thermal uniformity. It has been gold-plated to prevent oxidation.*" (p. 35 of ref. [29]) The sample, containing the detector, is glued to the puck (see fig. 6) to optimize the thermal contact to the puck. The glue is GE Varnish.

3.2.2 Cryostat

The cryostat used in our experiment is a Physical Property Measurement System (PPMS) (serial no. V089). In this section we summarize the relevant information about the PPMS from p. 15-45 of the PPMS Manual [29], divided into three topics: 1) The construction of the PPMS in general, 2) the temperature regulation of the sample space, and 3) the placing of the thermometers.

A schematic overview of the PPMS probe construction is given in fig. 7. The probe of the PPMS contains the sample space, the cooling annulus and an insulation layer. The insert is placed in the sample space, so that the puck is in the socket on the bottom of the sample space. The sample space is surrounded by the cooling annulus. The total probe is surrounded by a helium reservoir. A region filled with reflective superinsulation is placed between the cooling annulus and the helium reservoir. There are two ways of thermal contact between the sample and the cooling annulus: via the socket and via the helium exchange gas. The puck makes direct thermal contact with the cooling annulus via the socket. The walls of the sample space maintain thermal contact with the sample via helium exchange gas. The sample space is filled with low pressure Helium gas.

The temperature of the sample is regulated by the helium in the cooling annulus. This information is given in the manual: "*Temperature stability is* $\leq$*0.2% for temperatures* $\leq$ *10 K and* $\leq$*0.02% for temperatures >10K.*" (p.

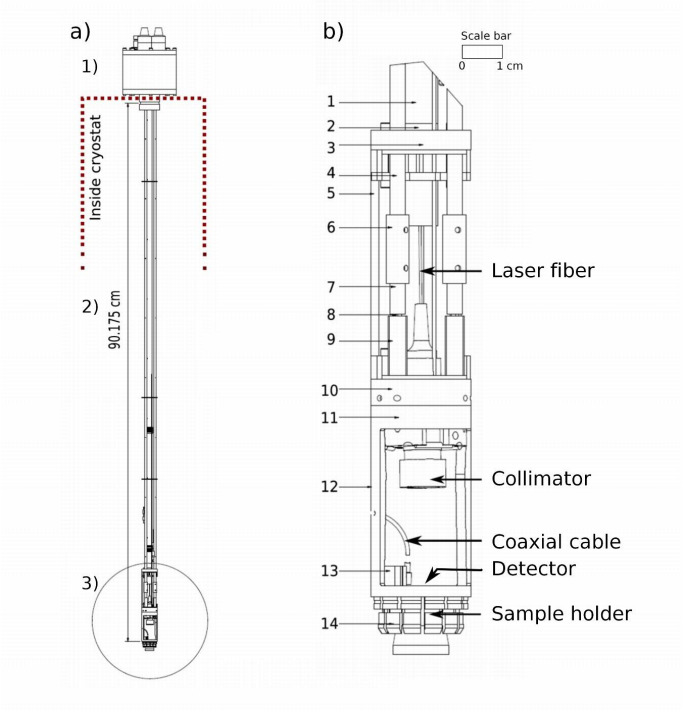

Figure 5: A drawing of the cryostat insert. a) A schematic overview of the insert. The insert consists of three parts, indicated in the drawing. The first part is placed outside the cryostat and contains the set screws to direct the laser beam, optical feedthroughs and a flange for sealing the vacuum in the cryostat. The second part contains the main tube for mechanical stability (stainless steel, OD: 9 mm, ID: 8 mm) and two mechanical feedthroughs (stainless steel, OD: 4 mm, ID: 3 mm), the laser fiber (section 3.3) and a coaxial cable (section 3.4.2). The maximal diameter is 26 mm. Part 3) is the lowest part of the insert, which is drawn in b) in more detail. The materials for the numbered parts are: 1,2,4,5,7-12: Stainless steel, 3,6: Polyether ether ketone (PEEK), 13,14: Gilded copper. The maximum OD is 26 mm. The most important parts are indicated in the figure. Part b) contains also the collimating lens which can be directed, PEEK heat barriers, the coaxial cable and the sample holder containing the detector (fig. 6). This picture is received from the FMD, Fijn Mechanische Dienst, LION, Leiden University.

15 of ref. [29]) In practice the displayed temperature regulation was stable within 0.002 K. There are two temperature regulation mechanisms, the 1) *high temperature mode* and the 2) *pot-fill mode*. In principal the first one is for temperatures above 4.2 K (Helium boiling point), the second is for lower temperatures.

1. Helium vapor is drawn in the cooling annulus. The temperature of the

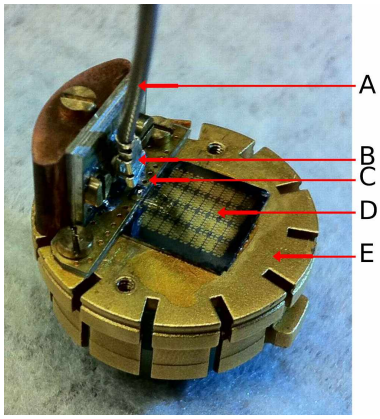

Figure 6: The sampleholder. The main parts are indicated in the figure. (A) is the UFL coaxial cable with a UFL connector (B) (section 3.4.2). The UFL connector is connected to a gold pad via a coplanar waveguide on an angled printed circuit board (PCB) (C). The PCB is connected to the detector on the chip (D) via a wirebond from the gold pad on the PCB to the signal pad on the sample. The detector is connected to the ground by a wirebond to the puck (E). The sample and the printed circuit board are glued to the puck with GE Varnish, so that the PCB and the sample make thermal contact to the puck. This is to ensure optimal thermal contact between the sample and the puck, to dissipate both the heat inflow from the UFL cable and the Joule heating in the detector.

vapor is regulated by the block heater below the sample space and the neck heater above the sample space. The amount of Helium vapor can be varied by the impedance tube.

2. The cooling annulus is filled with liquid helium. To cool down below 4.2 K the boiling point of the Helium is manipulated by decreasing the pressure by opening the flow-control valve. The temperature can be increased by closing the flow-control valve slightly and using the heaters eventually.

In practice the pot-fill mode can already be in use at temperatures below 7 K. Switching from the high temperature mode to the pot-fill mode takes extra time. The manual gives this information about that problem: "*The fill procedure is regulated by the pressure difference between the cooling annulus and the dewar. When the annulus is almost full, which takes about 45 minutes, the impedance heater is turned on, warming the impedance tube until the helium pressure inside the tube prevents liquid helium from entering either end.*" (p. 42 of ref. [29]) "*In the event you reset the temperature from below 4.2 K to above 4.2 K, it will take about 45 minutes to empty the*

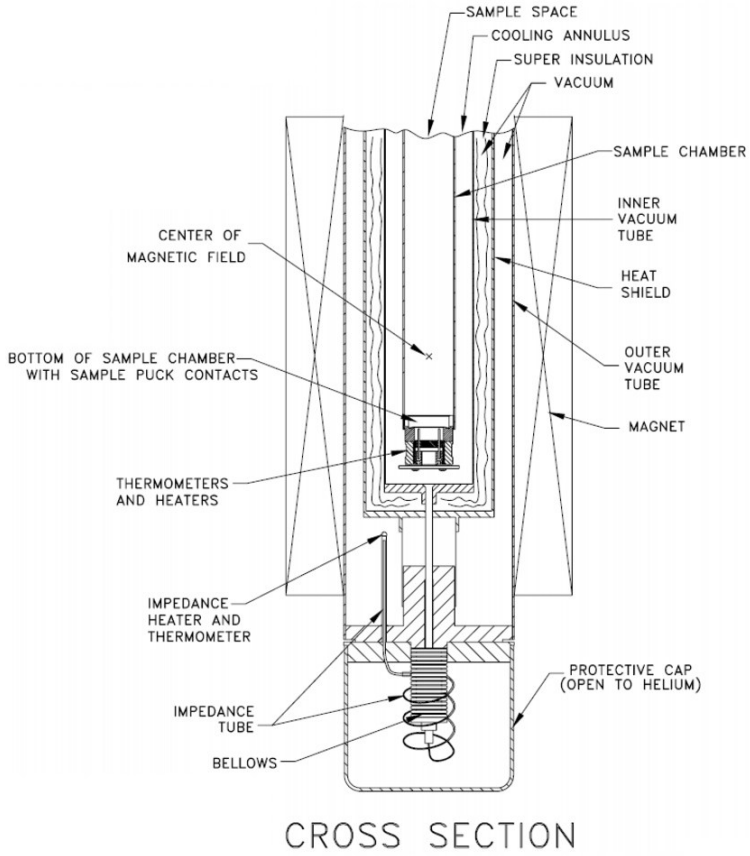

Figure 7: A schematic overview of the PPMS cryostat probe. The most important parts are indicated in the drawing. The insert is put in the sealed sample space, so that the puck is placed on the bottom of the sample space. The puck is placed in a socket on the bottom of the sample space. The socket is cooled by the Helium in the cooling annulus. The Helium flows to the annulus via a dual impedance system. The dual impedance system consists of two narrow tubes, which can be closed by heating the tube to form a Helium gas bubble. The magnet is not used in this experiment. The temperature is not measured on the sample, but by a thermometer immediately below the puck in the socket. This picture is taken from p. 28 of the PPMS Manual.[29]

cooling annulus. During this time, the system cannot control temperature in the sample space." (p. 43 of ref. [29]) In practice the temperature cannot be controlled for up to an hour, when the system is switching from the pot-fill mode to the high-temperature mode.

The placing of the thermometers turns out to be important for our experi-

ment, because the sample temperature can be different from the temperature of the thermometer. Three thermometers are placed in the PPMS. The most important one is a negative temperature coefficient (NTC) thermometer directly below the puck socket, so that the thermometer temperature should be very close to the temperature of the sample. The second thermometer is a platinum resistance thermometer for the high temperature regime (80 K - 400 K). The third thermometer is an NTC-thermometer, placed above the sample space to control the temperature gradient in the sample space. In our measurements the direct temperature values are measured by the NTC-thermometer in the socket. According to the manual, the temperature measurement accuracy is approximately 0.5% (p. 15 of ref. [29]).

3.2.3 Heat flow

The heat flows through our setup can be crucial for our experiment. The temperature of the device must be stable at temperatures of approximately 5 K, while the device is connected to the insert and to a bias current source outside the cryostat. In this section we describe our quantitative approach of the different heat flows.

There are two heat flows into the sample: through the coaxial cable and through the frame of the insert (fig. 5). Furthermore, there are three heat flows away from the detector: via the Helium exchange gas, via the wirebonds and through the socket (see fig. 7). The heat flows are defined quantitatively by (p. 514 of ref. [16]):

$$\dot{Q} = \frac{A}{L} \int_{T_1}^{T_2} \lambda dT, \tag{4}$$

where λ(T) is the temperature-dependent thermal conductivity, A is the cross-sectional area, L the length and T the temperature.

We give an approximation of three values: 1) The heat flow through the insert, 2) the heat flow through the cabling and 3) the cooling power of the PPMS. Notice that there are important differences between these theoretical calculations and the heat flows in reality. Furthermore, we assumed that the system is in equilibrium, but the cooling down time is not negligible (for instance the cooling of insulation of the coaxial cabling).

1. The heat flow through the insert passes four parts in series: The stainless steel tubes (numbered 2 in fig. 5a), the PEEK layers (numbered 3 and 6 in fig. 5b), the stainless steel below the PEEK layers (numbered 10-12 in fig. 5b) and the puck (numbered 14 in fig. 5). The PEEK

Temperature (K) above PEEK layer	$\int_{T}^{300K} \lambda dT$ (kW/m)	$\dot{Q}$ (mW)
250	0.72	61.5
200	1.40	120
180	1.65	141
160	1.89	161
140	2.12	181
120	2.33	199
100	2.53	216

Table 1: Theoretical heat flow through the three stainless steel tubes in total. The values are taken from p. 514-515 of ref. [16].

layers form heat barriers, so that there is no direct contact via stainless steel between the sampleholder and the part outside the cryostat.

The value of this heat flow can be approximated by calculating the theoretical heat flow through the three tubes relative to the temperature at the end of the tubes directly above the PEEK layer. The results are shown in table 1. In this model situation the three separated tubes make thermal contact to a heat reservoir at 300 K at one side and at the other side to a heat reservoir at the temperature given in the first column in table 1. We expect that the temperature above the PEEK layer ranges between 100 K and 250 K. The cooling by the Helium exchange gas is not taken into account.

2. The heat flow through the cabling can be approximated by the model situation, wherein the center conductors of the cabling are connected in series. The beginning of the first wire is connected to a heat reservoir at 300 K and the end of the last wire is connected to a heat reservoir at 4 K.

   The specifications of the inner conductors are given in section 3.4.2. The consecutive conductors are: the semi-rigid cable (approximate length: 70 cm; approximate thermal conductivity 50 $\mathrm{Wm^{-1}K^{-1}}$[30]), the UFL-cable (approximate length: 30 cm; approximate thermal conductivity 401 $\mathrm{Wm^{-1}K^{-1}}$[31]), the PCB (approximate dimensions: 1.1 x 2.2 cm; approximate thermal conductivity 401 $\mathrm{Wm^{-1}K^{-1}}$[31]) and the wirebond (approximate length 0.5 cm; approximate thermal conductivity 318 $\mathrm{Wm^{-1}K^{-1}}$[32]). The heat flow through the cabling is in this case 11 ± 1 mW.

   In this model situation the cables don't make thermal contact to the

surrounding materials. In reality the conductors are surrounded by isolation material and the outer conductors; the connection between the semi-rigid cable and the UFL cable is connected to the tube; the PCB makes thermal contact to the puck and the cabling is cooled by the Helium exchange gas.

We expect that the main part of the heat flow through the cabling will flow to the puck via the PCB. Only a small part will reach the sample via the wirebond.

3. The cooling power of the cryostat can be approximated by the amount of consumed Helium. A typical used Helium gas quantity is 1.4 L/min, as observed during the measurements. The evaporation of this gas amount requires 87 mW.[33] The heating of this gas quantity to room temperature provides much more cooling power, namely 6.35 W.

   We expect that the thermal contact between the puck and the socket will not reduce the heat flow to the socket. Therefore the temperature of the puck will be almost equal to the temperature in the socket (ΔT < 0.1 K).

We expect on the basis of these calculations that the heat flow to the socket will not exceed the cooling power of the cryostat. Temperature measurements on the puck are needed to ensure this expectation.

In conclusion we expect that the difference between the sample temperature and the reported temperature by the cryostat ranges within a few Kelvin. The exact sample temperature remains uncertain, because the quality of the thermal contact between the sample and the puck is unknown.

Furthermore the quality of the thermal contact between the nanowire and its environment (the substrate and the resist) is unknown. The sample is heated by the heat flow through the wirebond and by the Joule heating of the resistive parts of the detector. More certainty can be obtained by experiments, for instance hysteresis measurements.

3.3 Future optical access

The optical access to the detector consists of three components: 1) The feedthrough into the vacuum sample space, 2) the optical fiber and 3) the collimating lens.

1. The insert has two optical feedthroughs, a single mode and a multimode feedthrough. Only one of the feedthroughs is currently in use. All connectors are of the type FC-PC. Another option would be to use an uninterrupted laser fiber. The top plate of the insert would have to be rebuilt to make this option available.

2. Our operating wavelengths are in the range 600 - 1500 nm. The detection efficiency of meander detectors is strongly polarization dependent (p. 85 of ref. [34]). There are two kinds of fibers available:

   - Polarization maintaining fiber, range: 770 - 1100 nm, in two parts: The part outside the cryostat is 5 meter, the bare part inside the cryostat is 0.9 m. Probably this fiber will guide wavelengths up to 1500 nm also, but strongly attenuated.
   - Polarization maintaining fiber, range: 970 - 1550 nm, in two parts: The part outside the cryostat is 5 meter, the bare part inside the cryostat is 0.9 m. This fiber will guide wavelengths below 970 nm also. However, the fiber is probably not polarization maintaining for wavelengths below 970 nm and it will also guide the two-lobe Hermite-Gauss HG10 mode.

3. Two kinds of collimators are available. The first collimator has a focal distance of 2 mm and an Anti-Reflection Coating (ARC) specified for 600-1050 nm. The second collimator has a focal distance of 11 mm, ARC: 650-1050 nm.

3.4 Bias current and read-out electronics

In this chapter we will give an description of the electrical circuit. The description is divided into three parts: 1) The electronic circuit in general terms, 2) the technical specifications in detail and 3) a short, technical description of the measurement system for the RF signal.

3.4.1 General description

An overview of the electrical circuit is given in fig. 8. The voltage divider contains a tunable voltage source V_{in} (range: -10 to 10 V) and a large resistance R_1 (300 kΩ). The typical current range in the detector is -8 μA to 8 μA. The dashed R_s (3 kΩ) is a shunt resistance. It can be used in later experiments to lower the current in the detector when it is in the normal state. In our experiments this resistance is removed, unless indicated otherwise.

The voltage is measured in V_2 and the current is measured by measuring V_3 over the small resistance R_2 (100 Ω). The main components of the bias tee are the coil L_{DC} (3,4 nH) and the capacitor C_{RF} (47 nF). R_3 (100 kΩ) and C_1 (47 nF) are added to obtain a flat transfer function. The distribution of the temperature differences of the conductors inside the cryostat induces a small voltage V_T, caused by the thermoelectric effect (section 4.4.1). The equivalent circuit of the detector consists of a switch, a resistance and a coil. When the switch is closed, the detector is in the superconducting state and when it opens, the detector has resistance R_N. The given value (R_N = 570 kΩ) for this resistance is measured at room temperature. The resistance is 780 kΩ at 5 K. The coil L_k (approximately 425 nH, p. 82 of ref. [34]) represents the kinetic inductance.[8] The RF signal behind the capacitance C_{RF} is amplified by three amplifiers, which are 50 Ω terminated to prevent reflections. V_{out} is connected to a pulse counter or a oscilloscope.

Without shunt-resistance the combination of the voltage source and the 300 kΩ resistance acts like a current source. This behavior would be perfectly in case of $R_N << 300$ kΩ. When the shunt-resistance is added the combination of voltage source and two resistors acts like a voltage source. This behavior would be perfect in case of $R_N >> 3$ kΩ.

3.4.2 Specifications voltage source, voltage meters and cabling

The inaccuracy of each of the resistances R_1, R_s and R_2 is 1%. V_{in} is set by a NI DAQPad-6015. This device has a voltage range of -10 to 10 V.[35] V_2 is measured by a Keithley 2000 multimeter. The Keithley voltage measurement inaccuracy is close to negligible in our measurements. (Typical value: V_{in}= 5 V gives $V_2 = 2 \pm 0.0003$ V).[36] V_3 is measured by an Agilent 34410A.

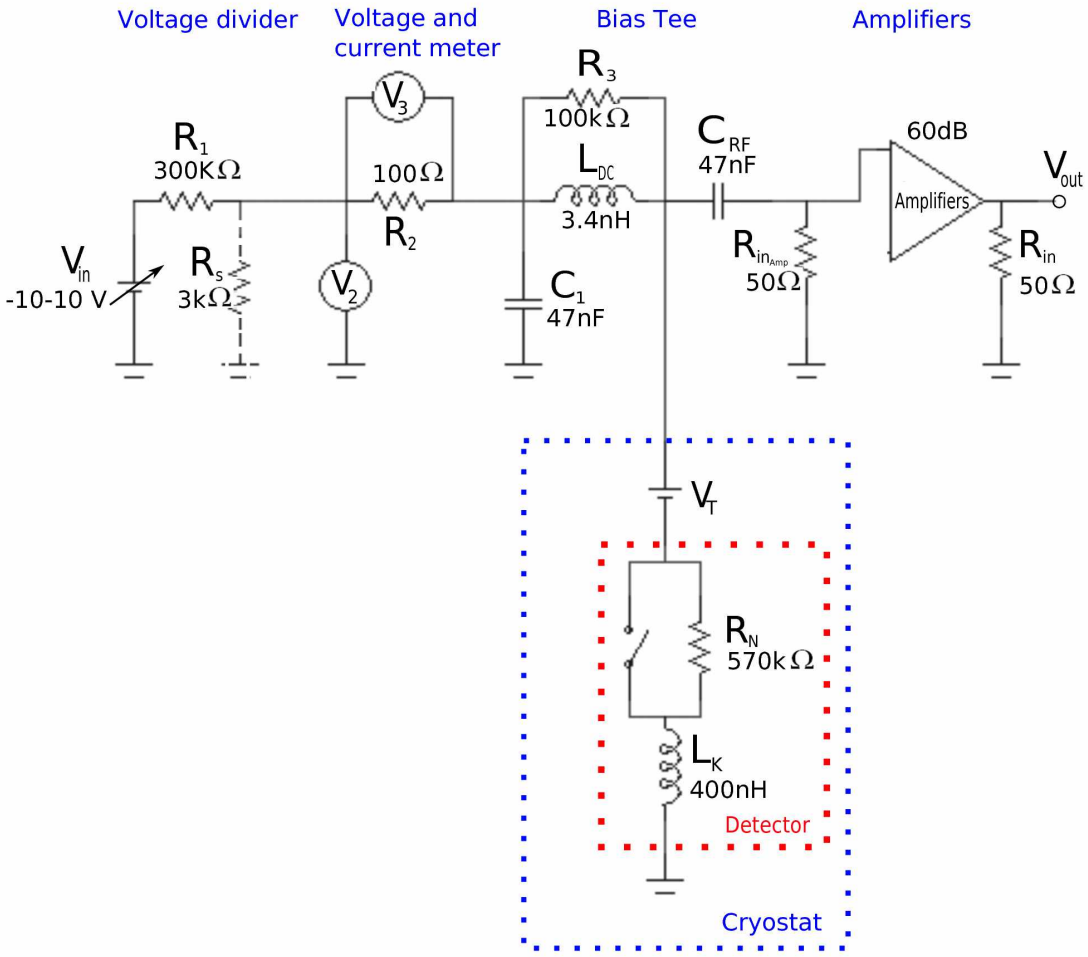

Figure 8: The electric circuit. The left side shows the current source. It provides a current bias to the detector. The detector produces a signal at ∼1 GHz. The measurement system for the RF signal is shown at the right side. The bias tee in the middle separates the DC from the RF signal.

The Agilent voltage measurement inaccuracy is close to negligible in our measurements, except at very low voltages ($V_3 < 0.1$ mV, see fig. 11). (Typical value: $V_{in} = 5$ V gives $V_3 = 0.9 \pm 0.005$ mV).[37] The pulses are counted by an Agilent 53131A Pulse Counter. Its trigger level is adjustable stepwise (stepsize: 5 mV).[38][39]

Different cable types occur in the circuit. V_{in}, V_2, V_3 and V_{out} have BNC connectors. The other connections outside the cryostat comprise (high-

frequency) SMA cables and connectors. The coaxial cable inside the insert consists of two parts. The first part of the cable, from the room temperature range to approximately 30 cm above the sample, is a coaxial semi-rigid cable (production nr. SC-086/50-SCN-CN; center conductor diameter: 0.203 ± 0.013 mm, material: silver plated cupronickel). The second part is a coaxial UFL-cable (production nr. U.FL-2LP-5016-A-(L) (or: (since a few years) U.FL-2LP-088N1T-A-(L))[40]), center conductor diameter: approximately 0.2 mm, material: silver plated copper). The transition connection is anchored to the main tube, because we expect that thermal contact between the tube and this transition connection will improve the cooling process of the inner conductor in the coaxial cable. The UFL cable is connected to the PCB. The conducting part of the PCB consists of a copper trace (thickness: 0.018 mm) and a gold pad. The gold pad and the signal pad of the detector are connected via a wirebond (gold, diameter: 25 μm). The second signal pad of the detector is connect to the puck via a wirebond. The puck is connected to the ground.

3.4.3 Spectrum analysis: Bias tee and amplifiers

The prediction of the amplitude of the photon absorption signal is described by Kerman *et al.*[8] In that paper the simple assumption is made, that the current through the detector in the normal state is negligible. The coaxial cable can be represented by a resistance of 50 Ω at high frequencies (in our case >1 GHz). Therefore Kerman *et al.* concludes that the pulse amplitude is described by $V_{pulse} \approx I_{bias} \times 50\ \Omega \times G_{amp}$, where G_{amp} is the gain of the amplifiers.

Different measurements are done to characterize the bias tee (production nr.: ZNBT-60-1W+ (mini-circuits)). We used a commercial network analyzer ('Hewlett Packard 8719D', range: 50 MHz - 13.5 GHz). The bias tee separates the DC and AC (RF) signals. C_{RF} attenuates all the signals below 3 MHz.

The RF signal is amplified by three identical 20 dB amplifiers. There are six amplifiers available: 2x ZX60-6013E+ (mini-circuits) and 4x ZX60-3018G+ (mini-circuits). We will use these three amplifiers: 3x ZX60-3018G+. Each amplifier is 50 Ω terminated. Different measurements are done to characterize the amplifier chain. The specified maximum output power (1 dB compression point) of each amplifier is 12.8 dBm. The behavior of the amplifiers near to this value is shown in fig. 9. We used a commercial spectrum analyzer ('ROHDE&SCHWARTZ FSC3', range: 9 kHz - 3 GHz) and the network analyzer 'Hewlett Packard 8719D'. The gain of the amplifiers is found to vary with the frequency of the signal (typical values: 1 GHz: 65,1 dB, 2 GHz: 60,6 dB). The specified maximum output power is exceeded when the

-50 dBm input power is amplified with more than 62.5 dB, see fig. 9. The gain is then attenuated (clipped) in the range 0 - 1 GHz.

Figure 9: Gain of the amplifier chain (containing three identical amplifiers). The horizontal axis is the frequency of the signal (range: 0 - 3 GHz). The vertical axis is the gain of the three amplifiers (range: 30 - 80 dB). The white line represents the gain at a input power of -50 dBm. Notice that the signal is compressed in the range 0 - 1 Hz, where the maximum input power is exceeded. For the yellow line a 10 dB attenuator is added to the circuit prior to the amplifiers. Notice that the yellow line shows the normal gain of the amplifier chain minus 10 dB. This graph is obtained by using the 'ROHDE&SCHWARTZ FSC3 Spectrum Analyzer'.

4 Critical current measurements

Several measurements have been done to determine the temperature-dependence of the critical current of the device. This chapter consists of four parts: 1) A description of the measurement method, 2) the results of the measurements, 3) a discussion on the achieved results and 4) a postscriptum.

4.1 Method

The I-R curves are determined by measuring the different voltages at different values for the voltage source V_{in}. The form of the sweep of V_{in} is shown in fig. 10. The form of the sweep and the procedure were the same for all the critical current measurements. The range and stepsize varied; the values are given in table 2 for each temperature. The step duration is approximately 460 ms for all the measurements.

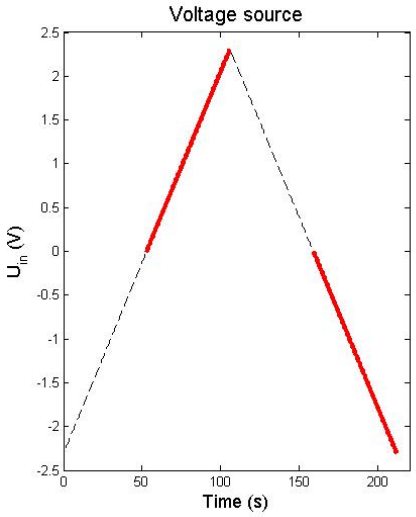

Figure 10: The set values of V_{in} for the measurements at 6 K. The value of V_{in} is plotted on the vertical axis as function of the time duration. The voltage set by the voltage source increases from -2.5 V up to 2.5 V and decreases thereafter to -2.5 V with constant stepsize. Each step takes approximately 460 ms. The resulting I-R curve is the result of the voltage measurements at the two red parts of the loop (from zero to the maximum voltage and from zero to the minimum voltage); we average the absolute voltages measured at the same absolute values for $+V_{in}$ and $-V_{in}$ to remove the influence of the thermo-electric effect (see section 4.4.1).

	Voltage source	
Temperature (K)	Stepsize (V)	Range (V)
2.88	0.025	-2.5 - 2.5
4.5	0.025	-2.5 - 2.5
5.0	0.020	-2.3 - 2.3
5.5	0.020	-2.3 - 2.3
6.0	0.020	-2.3 - 2.3
6.5	0.025	-2.5 - 2.5
7.0	0.025	-2.5 - 2.5
7.5	0.020	-2.5 - 2.5
8.0	0.020	-2.0 - 2.0
8.2	0.020	-2.0 - 2.0
8.4	0.020	-2.0 - 2.0
8.6	0.020	-1.5 - 1.5
8.8	0.020	-1.5 - 1.5
9.0	0.010	-1.0 - 1.0
9.2	0.010	-0.7 - 0.7
9.4	0.005	-0.5 - 0.5
9.6	0.005	-0.5 - 0.5
9.8	0.005	-0.5 -0.5
10.0	0.005	-1.0 - 1.0
10.1	0.005	-0.2 - 0.2
10.2	0.005	-0.2 - 0.2
10.25	0.020	-2.0 - 2.0
10.3	0.005	-0.2 - 0.2
10.4	0.005	-0.2 - 0.2
10.5	0.020	-2.0 - 2.0
10.5	0.005	-0.2 - 0.2
10.75	0.020	-2.0 - 2.0
10.75	0.020	-2.0 - 2.0

Table 2: Measurement specifications.

4.2 Measured I-R curves

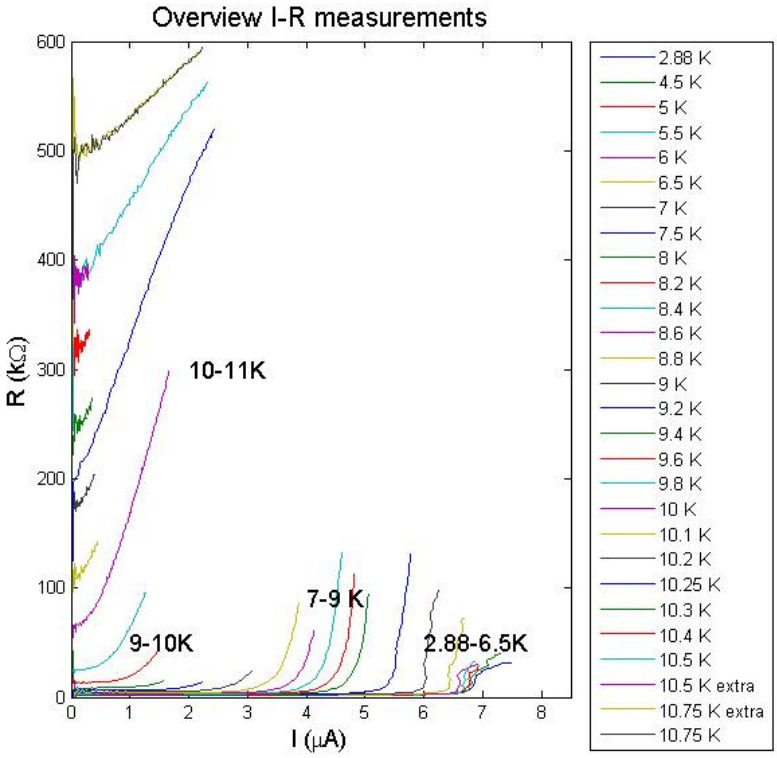

Figure 11: Resistance of the detector and the cryogenic probe as function of the bias current. The various lines indicate the resistance at different temperatures. These results are obtained by measuring the two voltages as described in fig. 8 and by applying the procedure described in section 4.1. The nonlinear behaviour is typical of superconductors. The noise at <1 μA is caused by inaccuracy in the current and voltage measurements at low values. More details and interpretation are given in the figures 12-15.

An overview of all the measured I-R curves is given in fig. 11, while the figures 12-15 present detailed views over specific ranges.

In general all the curves show the same behavior. Below the critical current the device is completely superconducting. The offset resistance is discussed in section 4.4.2. Above the critical current, the resistance of the device increases rapidly to the normal-state resistance. The critical current increases with decreasing temperature. The device does not show a state of complete superconductivity at temperatures above the critical temperature.

The critical temperature is reached at approximately 10 K. The fluctuation noise at low bias current (<1 μA) is due to the inaccuracy of the voltage meters.

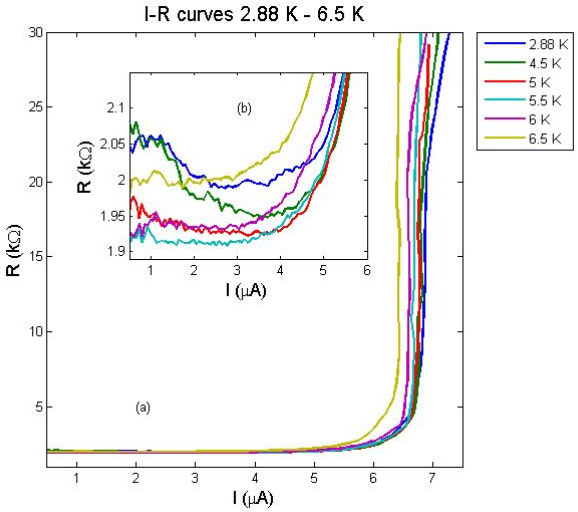

Figure 12: Resistance as function of the bias current. a) This figure is a zoom-in of fig. 11 at the temperature range 2.88 K - 6.5 K. b) The inset is a zoom-in of the offset resistance. Notice that the critical current stays almost constant at the temperature range 2.88 - 6 K (discussed in section 4.4.4).

The I-R curves for the temperatures 2.88 - 6.5 K are shown in fig. 12. Notice the remarkable behavior at the temperatures below 6 K. At these temperatures the resistance in the superconducting state does not decrease and the critical current seems to be constant. The resistance in the superconducting state at the lowest temperatures increases more with decreasing temperature at <2 μA than at 2-4 μA. Notice that the differences amount only a few percent of the total offset resistance. The offset resistance is discussed in section 4.4.2.

The I-R curves for the temperatures 7 - 9 K are shown in fig. 13. The decrease of the critical current at increasing temperature is clearly visible in this graph. Notice that the transition from the superconducting state to the normal state is less sharp at higher temperatures. The growth of the resistance after the critical current becomes less steep as well. These phenomena are signatures of the BKT-transition (see section 2.1).

The I-R curves for the temperatures 9 - 9.8 K are shown in fig. 14. Notice that the critical current decreases almost to zero. The superconducting state is visible at 9.6 K. At 9.8 K the superconducting state is almost indiscernible.

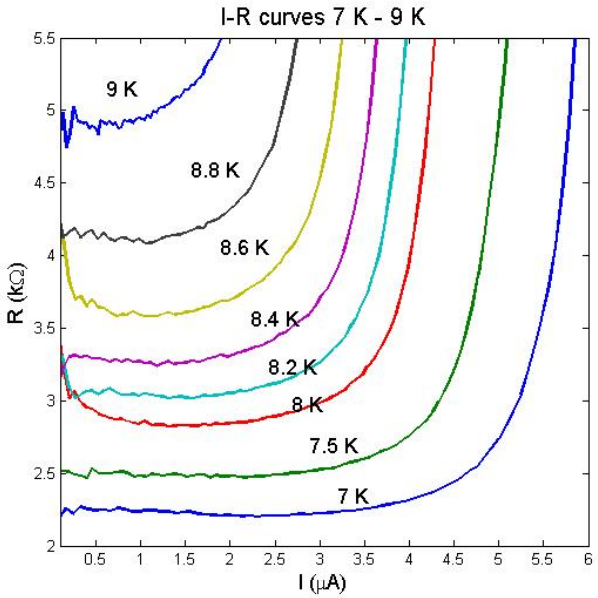

Figure 13: Resistance as function of the bias current. This figure is a zoom-in of fig. 11 at the temperature range 7 K - 9 K. The increasing offset resistance is discussed in section 4.4.2.

The I-R curves for the temperatures 9.8 - 10.75 K are shown in fig. 15. Above 10 K, the state of total superconductivity with constant resistance is not visible; the graph starts in the phase of growth of the resistance in the superconducting state to the normal state. The growth of the resistance seems to converge to approximately 600 - 800 kΩ.

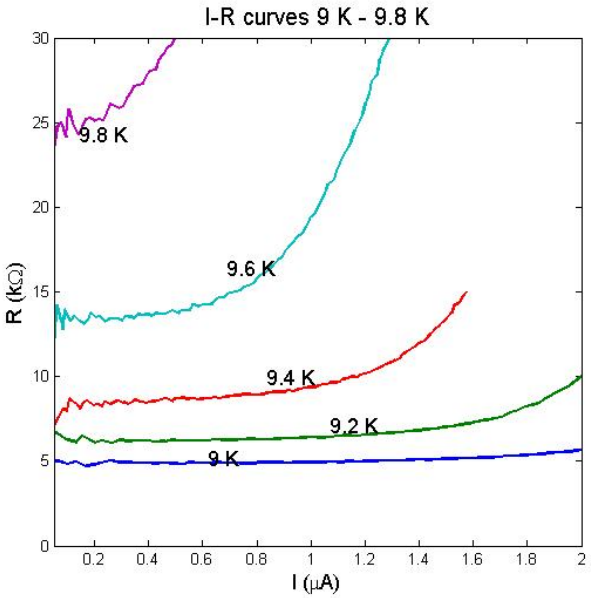

Figure 14: Resistance as function of the bias current. This figure is a zoom-in of fig. 11 at the temperature range 9 K - 9.8 K. The critical current approaches to zero; it is decreasing from approximately 1.8 μA to 0.5 μA.

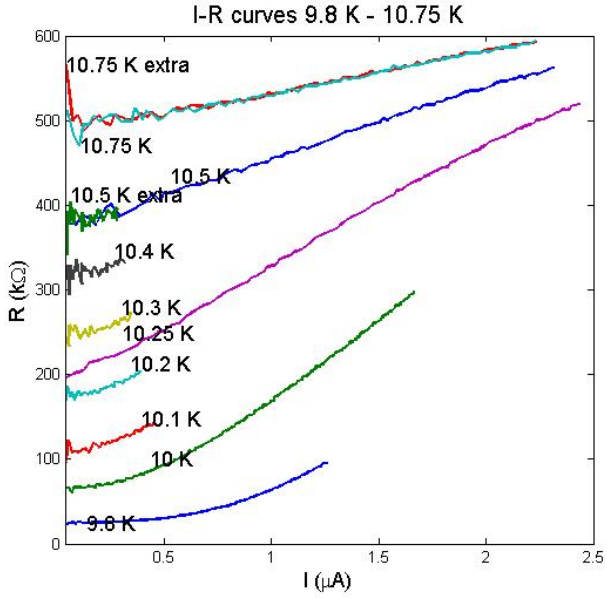

Figure 15: Resistance as function of the bias current. This figure is a zoom-in of fig. 11 at the temperature range 9.8 K - 10.75 K. Above 10 K there is no transition from the superconducting state to the normal state visible. The growth to the normal state resistance becomes less steep at higher temperatures.

4.3 Temperature-dependence of the critical current

The critical current can be determined by different criteria (see section 2.2). In this experiment the resistivity-criterion is used (see section fig. 16). We used different resistivity criteria: ΔR_{offset} = 1kΩ, 3kΩ, 6kΩ; represented by the green, red and blue line in fig. 16 respectively. Notice that the resistivity-criterion is applied relative to the temperature-dependent offset resistance. The result of this process: the temperature-dependence of the critical current, is shown in fig. 17.

In fig. 18 the experimental values are fitted with the theoretical curve τ, according to Bardeens theory (section 2.1). Our results are comparable to the results in the publication of Hofherr *et al.*[7]. Hofherr *et al.* measured the same linear behavior in the range between a certain temperature, in our experiment approximately 8.6 K ($\tau \approx 0{,}13$), up to T_C. The deviation for temperatures below 8.6 K is also measured by Hofherr. It is caused by a change in the behavior of the vortices (section 2.1). At temperatures below 6.5 K ($\tau \approx 0{,}5$) the critical current seems to be independent of the temperature. This behavior is not described in Hofherr *et al.* We discuss this behavior in section 4.4.

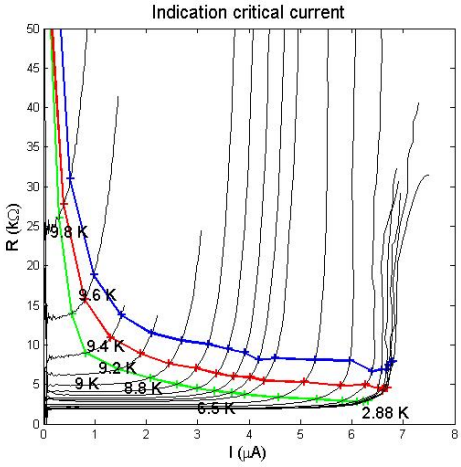

Figure 16: Critical current estimation. Resistance as function of the bias current. The black lines indicate the I-R curves as shown in section 4.2. The blue, red and green lines indicate the critical current at different temperatures as given by different offset criteria. The green, red and blue line represent the results of the offset criteria R_{offset} = 1kΩ, 3kΩ, 6kΩ respectively. The data points are obtained by applying the resistivity-criterion procedure described in section 2.2.

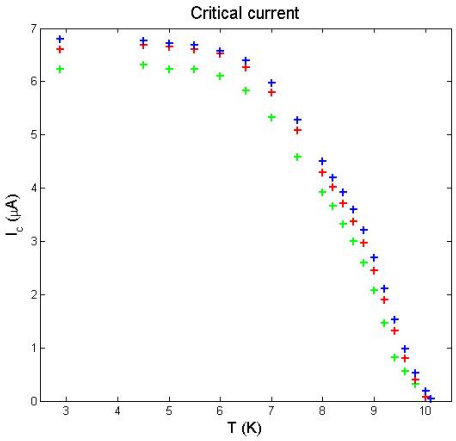

Figure 17: Critical current as function of temperature. The various lines indicate the same criteria as used in fig. 16 (indicated by the same colors). From this graph, we conclude that the critical temperature $T_c \approx 10 \pm 0.2$ K.

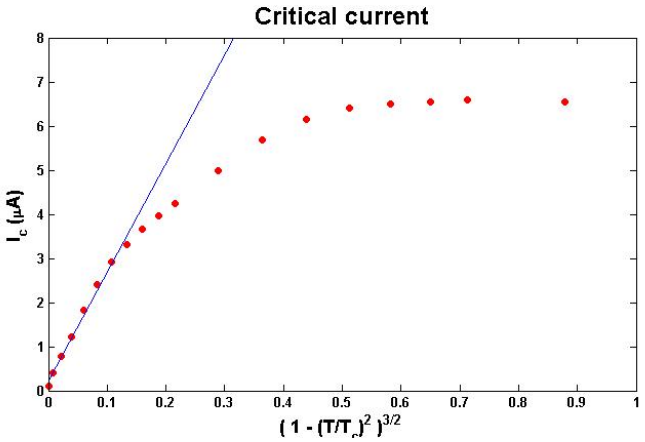

Figure 18: The temperature-dependence of the critical current. The critical current is plotted as function of $\tau = (1 - t^2)^{\frac{3}{2}}$, where $t = \frac{T(K)}{T_c}$ and $T_c = 10$ K. The critical current (symbols) are the averaged values from fig. 16. The solid line represents the linear fit through the data points for the temperature range 8.6 - 10 K ($\tau \approx 0$ - 0.13).

4.4 Discussion

This section contains the discussion of the critical current measurements. The discussion consists of four parts: 1) The elaboration of the correction for the thermo-electric effect, 2) the discussion of the measured offset resistance in the superconducting state, 3) a description of the bias current noise and 4) an evaluation of the temperature regulation.

4.4.1 Correction for the thermo-electric effect

The measurement procedure is described in section 4.1. The differences between the voltage measurements for positive voltage source values and for negative values, due to the thermo-electric effect, are shown in fig. 19. The average values are shown in fig. 20. This report does not elaborate further on the interpretation of these results.

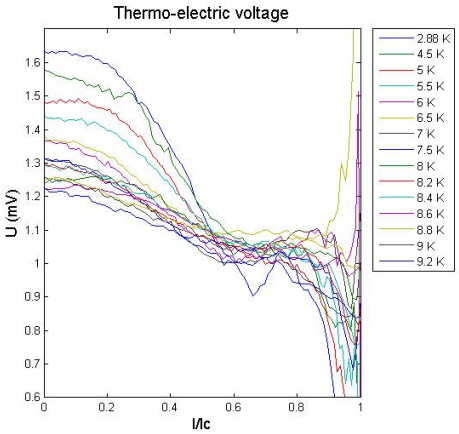

Figure 19: The voltage caused by thermo-electric effect as function of the bias current, normalized to the critical current. The different lines indicates the thermo-electric voltage at different temperatures. The data points are obtained by taking the difference between the voltages in the positive range and the negative range (see section 4.1). The critical current is determined by using the 3kΩ offset-criterium (see fig. 16).

4.4.2 Offset resistance

All our measurement results show a resistivity in the superconducting state (except the voltage-biased measurements, that we performed later, described in section 5.3). The values of this resistivity are given in fig 21. Notice

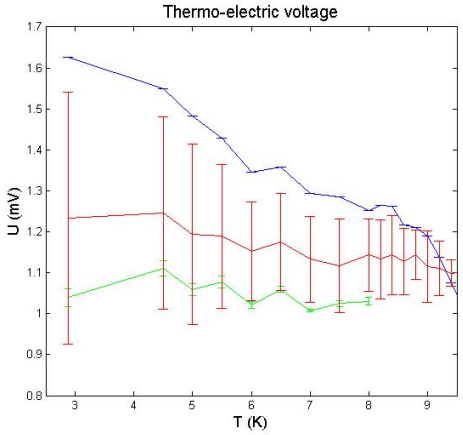

Figure 20: The thermo-electric voltage as function of the temperature. The blue line represents the voltages in the I_{bias} range 0.1 to 1 μA. The data points represented by the red line are obtained by taking the average of all the thermo-electric voltages from 0.1 μA up to the critical current (see section 4.3). The green line represents the voltages in the range 4 - 5 μA. The errorbars are the standard deviations. Near 10 K the results becomes less reliable, because the critical current approaches zero at 10 K. The measurements above the critical current are less accurate, because of the increasing resistance of the detector. The critical current is determined by using the 3 kΩ offset-criterium (see fig. 16).

that this resistivity in the superconducting state seems to be temperature dependent but independent of the bias current level.

We assume that we have to solve this problem experimentally, therefore we do not spend more attention on the theoretical explanation.

Several measures have been taken to ensure that the extra resistivity is not caused by failures outside the device. The wirebond connections are replaced by double wirebonds. The UFL-cable is tested for failures at cryogenic temperatures, by measuring its resistance at room temperature and in liquid nitrogen. After these measures the device showed the same resistivity. A remaining possibility is a failure in the connection between the signal pads of the device and the nanowire. The only way to exclude this possibility is to repeat the measurements with another detector.

The resistance disappears in the voltage-biased measurements, described in section 5.3. The differences in the set-up were:

- The bias tee and the amplifiers were added to the system for the voltage-biased measurements. This affects the bias voltage noise level.
- The insert had been in the cryostat 24 hours longer for the voltage-

biased measurements than in the previous measurements. This may result in a different temperature regulation.

The consequences hereof are uncertain and specific measurements are needed.

The Joule heating due to this offset resistance, given by

$$P = I_{bias}(t)^2 R(t), \tag{5}$$

is small in comparison to the total heat flow to the sample. A first estimate (R = 2 kΩ, I_{bias} = 5 μA) gives a heating power of 5 x 10^{-5} mW.

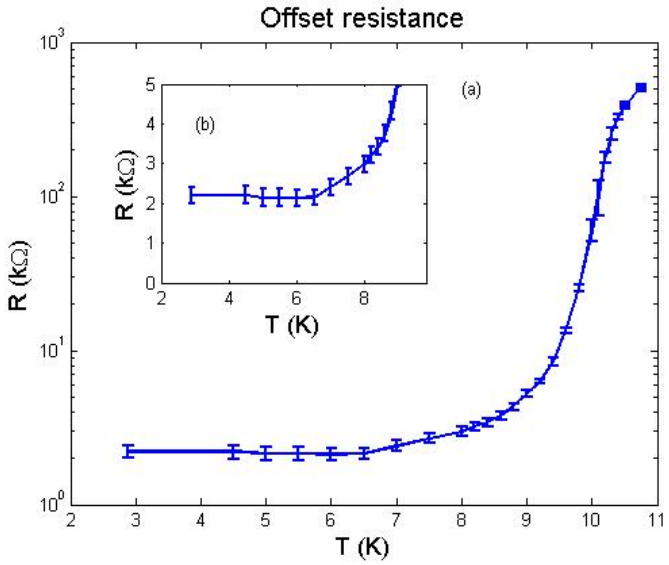

Figure 21: The combined resistance of the superconducting detector and the electronic circuit in the cryostat as function of the temperature. a) The logarithm of the resistance is plotted on the vertical axis. Each data point is obtained by reading the resistance in the curves given in fig. 11. b) The same data in the range of 2 - 10 K but with a linear vertical axis. Notice that the graph becomes remarkably flat at temperatures below 6 K.

4.4.3 Johnson noise

The noise produced by the resistances, especially the 300 kΩ resistance, seems to be important for our measurement (section 4.4.2). We conclude this from the differences between the measurements where the detector is shielded against the noise from the 300 kΩ resistance and the measurements where the detector is not shielded. The detector is shielded in the voltage-biased measurements where the bias tee is added to the circuit. The offset

resistance disappeared when the bias tee is added. We are not sure about the causality of this relation.

Johnson noise influences the experimental critical current values. This is described by J. W. Ekin: "*Aside from generating voltage noise, current oscillations can also reduce the apparent dc critical current. As a general rule, a sinusoidal current ripple of a given percentage will reduce the apparent* I_c *by about the same percentage (Goodrich and Bray, 1988).[41] For example, a sinusoidal current ripple that is 1% of the dc current (or a* peak-to-peak *amplitude of 2%) will reduce the measured critical current by slightly less than 1%.*"(p. 362 of ref. [16])

The Johnson noise is described by:

$$I_{noise} = \sqrt{\frac{4kT\Delta\nu}{R}}, \tag{6}$$

where k is the Boltzmann constant, T the temperature, $\Delta\nu$ the band width and R the resistance. A first estimate (T = 300 K, R = 300 kΩ, $\Delta\nu$ = 1 GHz) gives $I_{noise} = 0.0074$ μA.

4.4.4 Temperature regulation reliability

At temperatures below 6.5 K the offset resistance remains constant (see section 4.4.2) and the critical current remains almost constant (see section 4.3). A possible explanation for this behavior is that the temperature regulation has failed, so that the temperature of the device has been constant when the measured values of the temperature were <6.5 K. This would also mean that all the temperature measurements are unreliable.

4.5 Postscriptum

From further measurements performed after the completion of this work, it has become apparent that by reducing the bias resistor R_1 from 300 kΩ to 2 kΩ, the behavior of the device conforms to that of literature.

There are two possible explanations for this effect: either the noise properties of the resistor affect the IV curves, as discussed in section 4.4.3, or the large resistance causes the device to latch.[23][42]

5 Self-heating hotspots

In this chapter, we show the device resistivity in case of a bias current level above the critical current level. The chapter consists of four parts: 1) A general description of the current-biased measurements, 2) a closer look at the influence of the geometry of the detector, 3) a description of the voltage-biased measurements and 4) a brief discussion of the measurement errors.

5.1 Measured hysteresis and step behavior

We vary the input voltage in a sweep upwards from 1.5 V up to 5 V and downwards from 5 V to 1.5 V ten times in succession (stepsize: 50 mV, step duration: 459 $\pm$ 5 ms). The results are obtained by measuring the two voltages as described in fig. 8 and applying the procedure described in section 3.4. The resulting resistance is described by:

$$\frac{V_2}{I_{bias}} = \frac{V_{in}}{I_{bias}} - (R_1 + R_2), \tag{7}$$

All the measurement points will be distributed over the curves of constant total voltage over the whole circuit, whereby the distance between the curves is determined by the stepsize of the input voltage. This effect will be visible in these measurements, because we measure more times at the same bias current level, in contrast to the measurements in chapter 4. The results are not corrected for the thermo-electric effect. The measured temperature was 3.1 K. We expect that the real temperature was between 3 K and 6 K (see section 4.4.4).

An overview of the measured sweeps is given in fig. 22. During the ramp up the resistance of the device increases incrementally from the resistance in the superconducting state up to approximately 300 kΩ. At low current (<5.2 μA) the device is superconducting (1). Above the critical current the resistance increases until one or two of the branches of the detector (see section 3.1) are in the normal state (2). The bias current increases after the first steps (3) again until the critical current is reached in one of the other branches (4). It is reasonable to assume that the edges of the nanowire form an obstruction for the expansion of the normal area. The critical current is not reached at the edges, because the nanowire is wider at these areas. The expansion within the branches, caused by the Joule heating, is faster than the measurement process, so the expansion within one branch cannot be measured in real time. Therefore, the measured resistance of the nanowire increases by steps of the size of the resistance of one branch. This process is repeated (5,6,7,8,9) for each next branch. Notice that the resistance makes

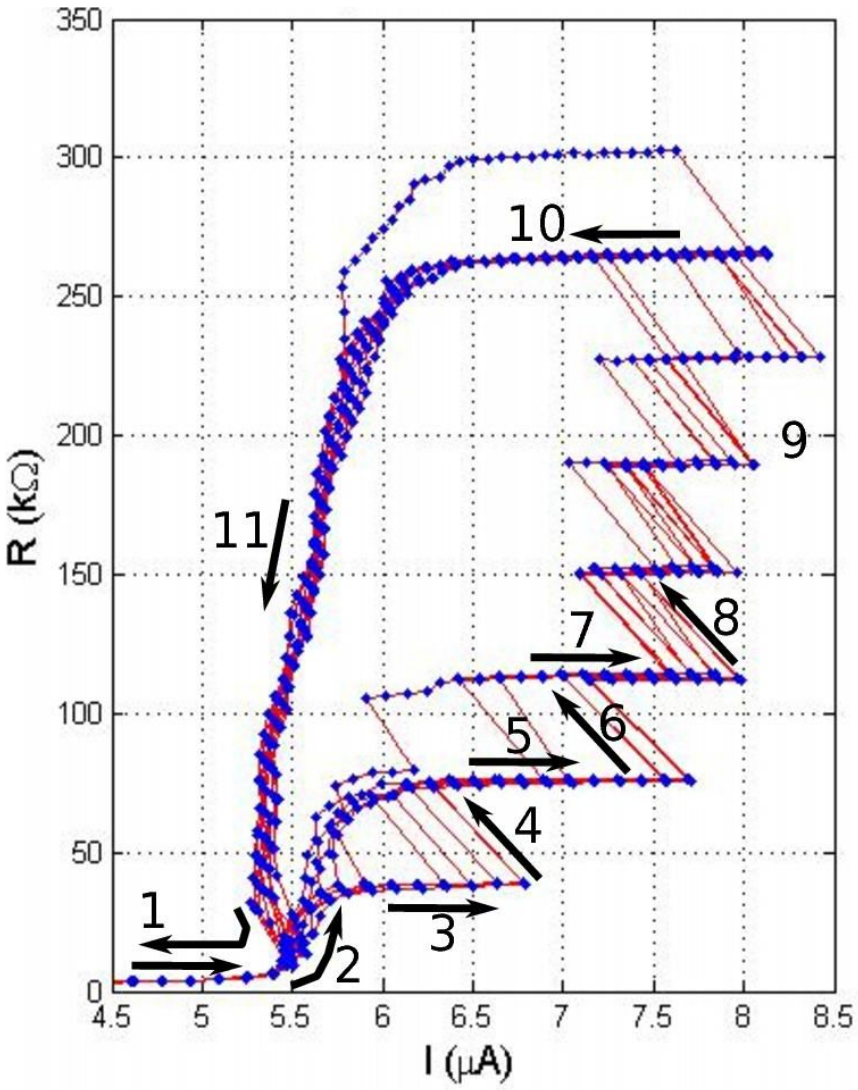

Figure 22: Resistance of the detector and the cryogenic probe as function of the bias current. The various lines indicate different loops. The arrows in the figure indicate the evolution of the resistivity. The bias current has been increased and decreased ten times by increasing and decreasing V_{in} ten times in the range 1.5 - 5 V. More details are given in the figures 24-30.

an extra step in one of the loops. During the ramp down, whereby the input voltage decreases, the resistance remains constant (10) until it decreases rapidly (11) to the superconducting state (1). The resistance is higher in the ramp down than in the ramp up. These measurements show no step behavior in the ramp down.

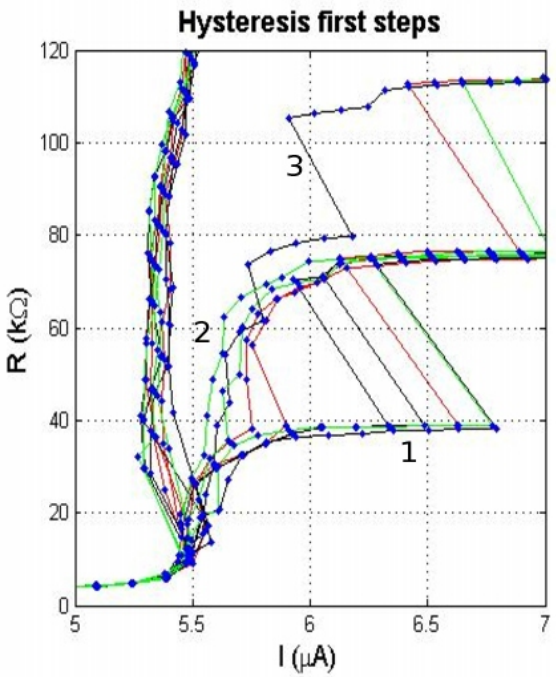

Figure 23: Resistance as function of the bias current. This figure is a zoom-in of fig. 22. The first three loops are indicated by red lines, the loops 4-7 are indicated by black lines, the loops 8-10 are indicated by by green lines. Notice that there is no clear relation between the number of the loop and the behavior of the resistance.

Fig. 23 shows the behavior of the resistance during the transition to the normal state of the first branches. In some loops the detector remains in the state with only one branch in the normal state for a longer time (1). In other loops the detector becomes resistive by smaller and more steps up to the state with two branches in the normal state. (3). This behavior may be caused by expansion of the normal state through the edges of the branches or by the heating of branches by the Joule heating of an adjacent branch. Notice that the resistance increases directly after the critical current by small steps. Further above the critical current level the resistance increases only by big steps. This behavior can be explained by mentioning the low level of the bias current. At this level (5.5 - 6 μA) the Joule heating around the hotspot is apparently not large enough for an expansion through the whole branch.

Fig. 24 shows the behavior of the resistance during the stepwise increase of the resistance. In this range the resistance increases only in large increments, equivalent to the resistance of single branches. The resistance steps

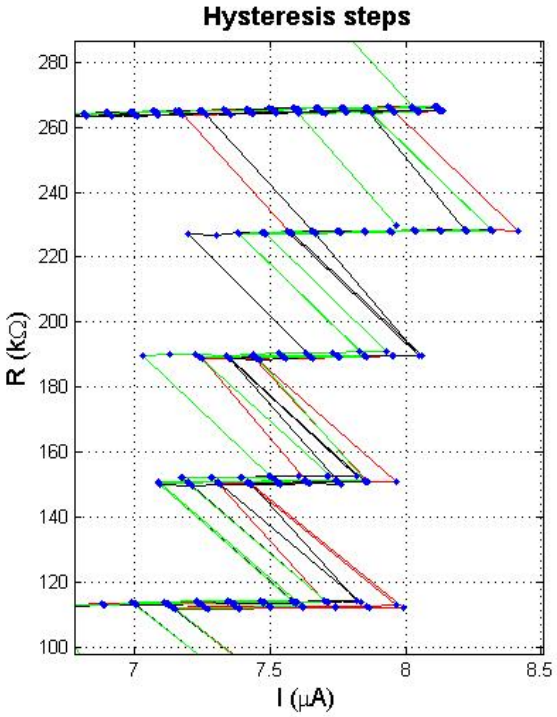

Figure 24: Resistance as function of the bias current. This figure is a zoom-in of fig. 22. The first three loops are indicated by red lines, the loops 4-7 are indicated by black lines, the loops 8-10 are indicated by by green lines. There is no clear relation between the number of the loop and the behavior of the resistance.

at current values which are for each step distributed over a range of approximately 0.5 μA (difference in bias current level between the first step and the last step) and in the last step even over a range of approximately 1 μA. This behavior has been investigated by Mattioli *et al.*[43] In general in each loop the subsequent steps seems to happen at a higher bias current, presumably because the first steps are caused by the tightest constrictions with the lowest critical currents. Notice that heating of adjacent branches can influence this behavior. In our measurements the average critical current for the first step/constriction is 5.5 μA and the average critical current for the 4th - 7th step is approximately 7.5 μA.

Fig. 25 shows the behavior of the resistance during the ramp down. Lowering of the critical current during a ramp down due to thermal coupling causes hysteresis. In the ramp down the results are spread over 0.05 - 0.1 μA and over 5 - 10 kΩ at equal source voltage.

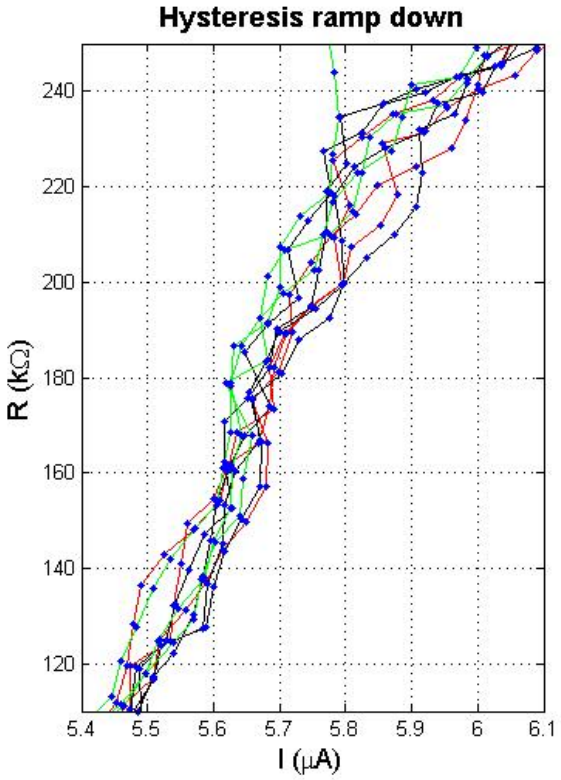

Figure 25: Resistance as function of the bias current. This figure is a zoom-in of fig. 22. The first three loops are indicated by red lines, the loops 4-7 are indicated by black lines, the loops 8-10 are indicated by by green lines. There is no clear relation between the number of the loop and the behavior of the resistance.

None of the figures 23 - 25 shows a relation between the number of the loop and the resistance behavior. Therefore we can conclude that these measurements have no significant lasting consequences for the detector.

We removed a few weird data points, which are presumably caused by errors in the voltage source or voltage meters. In fig. 26 the difference ΔV between the source voltage and the measured voltages is plotted as function of the bias current. ΔV is calculated by

$$\Delta V = V_{in} - I_{bias}(R_1 + R_{cabling}) - V_2, \tag{8}$$

wherein $R_{cabling}$ is the resistance of the cabling between V_{in} and V_2 (2 kΩ, approximated by minimizing $\sum_{I_{bias}} \Delta V$). There are some deviations above 6 μA. In our measurements the deviations larger than 50 mV are classified as errors.

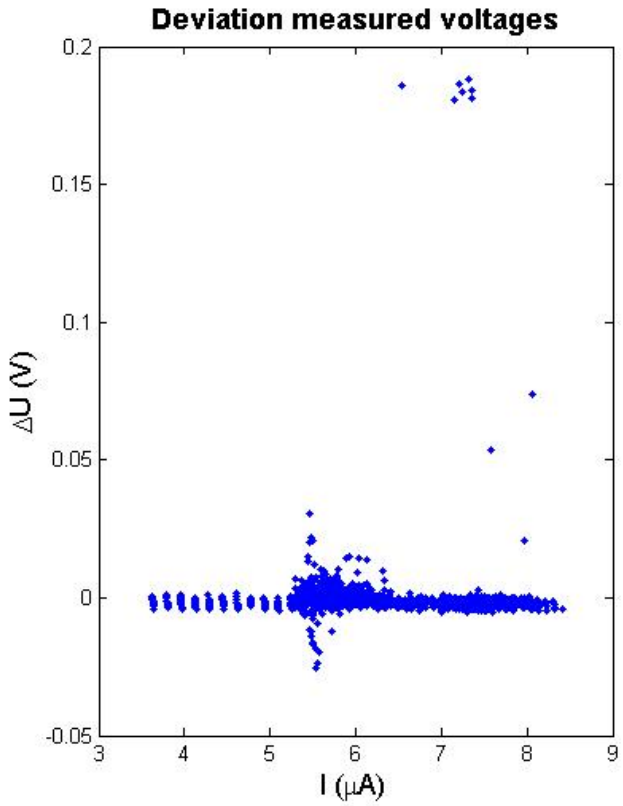

Figure 26: Measurement errors. The difference between V_{in} and the measured voltages in V_2 and V_3 (see section 3.4) is plotted as function of the bias current.

5.2 Closer look at step behavior

In this section the step behavior of the resistance is quantified. Fig. 27 shows the histogram of the resistance during the ramp up. Notice that the broad distribution of measurement points below 100 kΩ is caused by the continuous growth of resistance during some loops. The seventh peak is larger because a part of the measurement points in the ramp down is added. Only one of the loops reaches a resistance value above 300 kΩ.

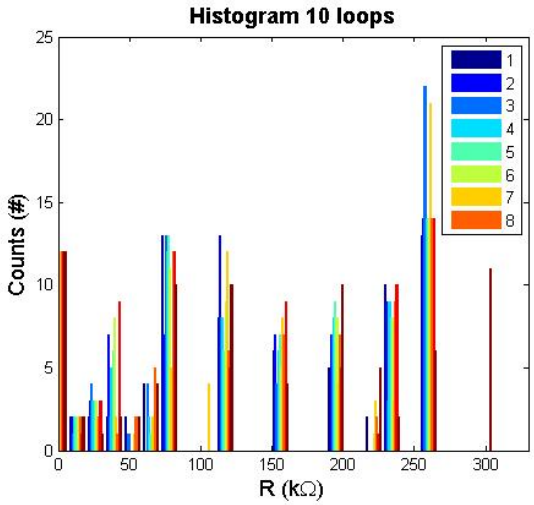

Figure 27: Histogram of the behavior of the resistance of the detector. The data points are obtained by using the ramps up in the hysteresis measurements. The histograms of ramps up of the hysteresis loops are plotted per loop against the average resistance of each level. The number of each loop is indicated by different colors, see the legend.

Fig. 28 shows the histogram of the seventh sweep of the bias voltage. Notice that the resistance increases quickly to the level of approximately 120 kΩ, as mentioned in section 5.1.

Fig. 29 shows the histogram of the tenth sweep of the bias voltage. Notice that the resistance increases quickly to the level of approximately 70 kΩ. This is the only loop that reaches a resistance above 300 kΩ, as mentioned in section 5.1.

Fig. 30 shows the sizes of the resistance steps. The size of the steps seems to decrease slowly with the step number, although the measurements are also consistent (albeit barely) with a constant stepsize.

The resistance of the detector in total at cryogenic temperatures is 780 kΩ. Therefore the average resistance of a single branch is 37.1 kΩ. The

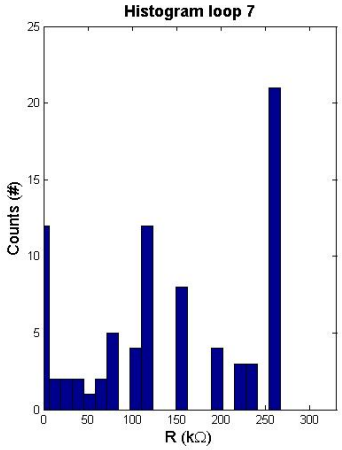

Figure 28: Histogram of the behavior of the resistance of the detector. This graph contains the data points of fig. 27 for only the seventh loop.

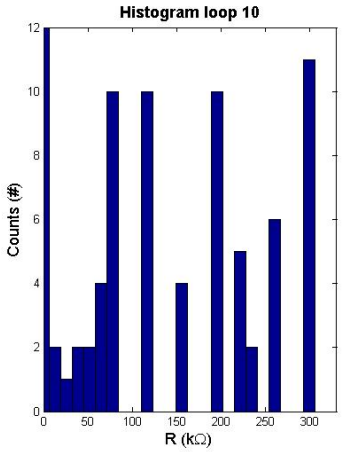

Figure 29: Histogram of the behaviour of the resistance of the detector. This graph contains the data points of fig. 27 for only the tenth loop.

variation in resistance for the other branches can be investigated by doing the same measurements for all the branches.

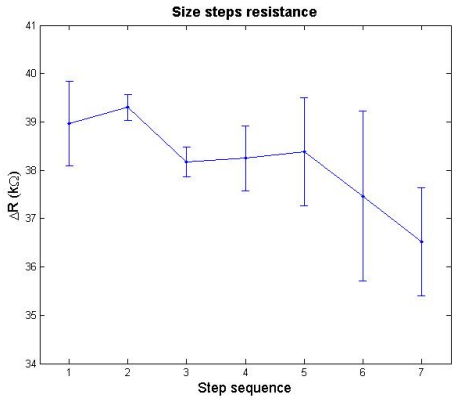

Figure 30: The step size between the resistance levels plotted against the number of the step. The error bars are obtained by calculating the standard deviation of of each level separately.

5.3 Stabilization of non-self-spreading hotspots

In this section we will show how a voltage-biased approach allows stabilization of a normal phase that grows discontinuously within a single branch, in contrast to the stepwise resistivity growth discussed in section 5.1. To reach a voltage-biased system instead of a current-biased system the shunt-resistance is added (see section 3.4). We now vary the input voltage in a sweep upwards from -10 V up to 10 V and downwards from 10 V to -10 V (stepsize: 20 mV, step duration: 459 $\pm$ 5 ms). The results are again obtained by measuring the two voltages as described in fig. 8 and applying the procedure described in section 3.4. The graphs are not shown in real time sequence. Fig. 31(a) contains the results in the sweep 0 - 10 V. Fig. 31(b) contains the results in the sweep 0 - -10 V. Fig. 32(a) contains the results in the sweep -10 - 0 V. Fig. 32(b) contains the results in the sweep 10 - 0 V. The results are not corrected for the thermo-electric effect. The thermo-electric effect causes an small difference ($\sim$ 1 - 2 mV) between the measurements at the positive and the negative V_{in} values.

Fig. 31(a) and 31(b) show the increase of the resistivity and bias current as function of the input voltage. In the superconducting state ($V_{in} < 3$ V) the bias current increases while the resistivity stays close to zero. Above the critical current the resistivity grows sometimes by steps and sometimes continuously. Both phenomena are mentioned in section 2.4.

We can compute the size of the resistive area by comparing the resistance to the values given in the figures 3 and 30: 1 kΩ corresponds to approximately 0.13 μm.

Probably the resistivity increase after the first step is caused by Joule heating of one hotspot: one uninterrupted part of a specific branch. The critical current is reached in one of the constrictions at a bias current of approximately 9.1 μA in fig. 31(a). All other constrictions in the device are still superconducting at this bias current level. As long as the bias current is below this level, resistivity increase is caused by expansion of the area in the resistive state by Joule heating. More measurements are needed to exclude that Joule heating caused transitions in adjacent branches.

Fig. 32(b) and 32(a) show the resistivity decrease and the bias current as function of the input voltage. The resistivity decreases sometimes continuously and sometimes by steps. The behavior during the ramp down differs from the behavior during the ramp up, as described in section 2.4.

The results during the ramp up are highly reproducible. The only difference between fig. 31(a) and fig. 31(b) is the step between 2.5 and 3 V. There are more and smaller differences between fig. 32(a) and fig. 32(b).

Our results are in agreement with the publications of Adam *et al.* [24]

and Elmurodov *et al.*[25]. To the best of our knowledge the observed reproducibility is a new result.

Hotspot-expansion contains information about the geometry of the constrictions in the detector, the Joule heating effect on adjacent branches and the thermal contact between the nanowire and its environment. Especially the ratios of the constrictions in the different branches can be studied in detail with this method. Finally this may contain information about the quality of the detector, as described in section 2.4.

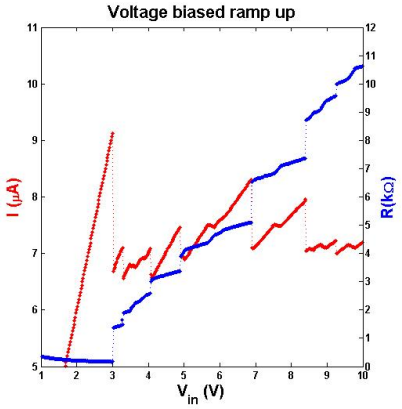

(a) Input voltage sweep: 0 to 10 V. This is the second quarter of the total sweep.

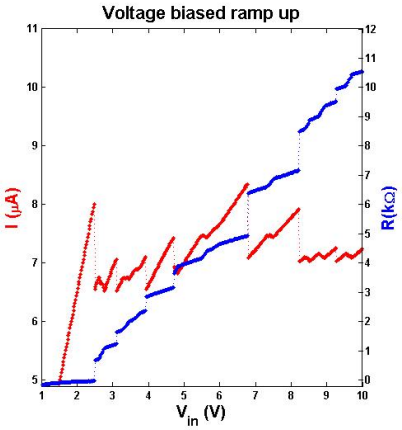

(b) Input voltage sweep: 0 to -10 V. This is the fourth quarter of the total sweep.

Figure 31: The increasing bias current and resistance in a voltage-biased system. The bias current is plotted in red (left vertical axis), the resistance is plotted in blue (right vertical axis), both as a function of input voltage. The absolute value of the input voltage is plotted on the horizontal axis.

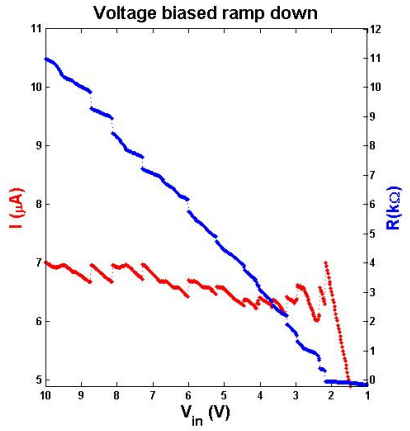

(a) Input voltage sweep: -10 to 0 V. This is the first quarter of the total sweep.

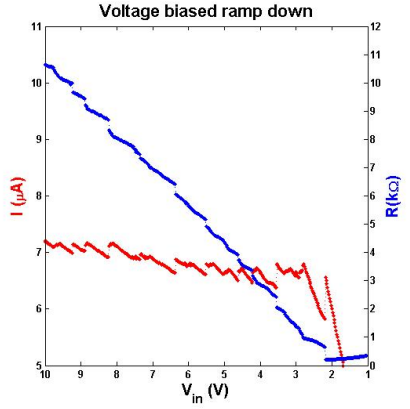

(b) Input voltage sweep: 10 to 0 V. This is the third quarter of the total sweep.

Figure 32: The decreasing bias current and resistance in a voltage-biased system. The bias current is plotted in red (left vertical axis), the resistance is plotted in blue (right vertical axis), both as a function of input voltage. The absolute value of the input voltage is plotted on the horizontal axis.

6 Conclusion and outlook

We have characterized the temperature-dependence of a NbN superconducting nanowire single-photon detector. Our main results can be summarized as follows:

First, we have investigated the critical current behavior and studied the influence of depairing vortices. We have measured I-R curves including a clear superconducting state and transition to the normal state at a wide range of temperatures. The critical current behavior is in agreement with the theoretical behavior, however, the absolute values may be unreliable because of the temperature regulation problems.

Secondly, we have investigated the self-spreading hotspot behavior in a current-biased system and a voltage-biased system. The hotspot-expansion contains information about the local width of the nanowire and the local thermal contact between the nanowire and its environment. We have shown that the detector transits from the superconducting to the normal state branch by branch in a current-biased system. In a voltage-biased system the detector transits in much smaller steps in a voltage-biased system. We have demonstrated highly reproducible stabilization of small hotspots in a voltage-biased system. To the best of our knowledge the reproducibility of the hotspot expansion is a new result. These demonstrated measurement techniques can give useful information about the detector geometry in a direct way. From the step behavior in a current-biased system, the resistances of the different branches can be determined. The limiting constrictions can be characterized by either analyzing the critical current for each branch (current-biased) and the hotspot expansion within one branch (voltage-biased).

We can give these recommendations to improve the setup:

- To measure the temperature properly, thermometers should be placed close to the sample on the puck.
- The use of thicker coaxial cables can be considered to prevent broken cables, because the heat flow through the cabling is small in comparison with the heat flow through the stick.
- The use of amplifiers with less frequency dependence of the gain would make it possible to reach high gain without exceeding the maximum input power of the last amplifier.
- In future measurements, the Johnson voltage noise of the 300 kΩ has to be reduced by using a smaller resistance or by using the coil in the bias tee as noise barrier.

- The strong polarization dependence of the detection efficiency of meander detectors (p. 85 of ref. [34]) requires polarization control or unpolarized light. Either depolarizing the laser beam or using polarization maintaining feedthroughs are difficult to realize. An uninterrupted optical access to the sample space, obtained by a 'vacuum pressure penetrating feedthrough'[44], may be a useful solution.

We recommend these future experiments:

- The temperature dependence of the critical current must be measured again with improved temperature measurement.
- It would be interesting to measure the total superconducting-normal transition of all the branches and the resistance of the whole detector at low temperature. This is a proper way to compare the distinguished branch resistances.
- To investigate the limiting constrictions of the detector, the hotspot spreading can be studied for a voltage-biased system over more then one branch. Thereby the reproducibility can be used to distinguish the different branches.

7 Acknowledgements

In the first place I would like to thank Jelmer Renema, my first supervisor, for always giving me the guidance and encouragement I needed, for teaching me how to do research and how to write a thesis and for always sharing his time for all kinds of questions. In addition, I would like to thank especially Martin van Exter, my second supervisor, for giving me very useful advice in all the parts of the project. I acknowledge also my unofficial supervisors, Michiel de Dood and Qiang Wang for their guidance, advice and patience. I am grateful to all the Quantum Optics group members, Leiden University, for offering me the opportunity to perform my bachelor project.

Furthermore, it is a pleasure to thank all the other people who made this project possible:

Dondu Sahin, from the TU/e, for the construction of the device and advice in their proper use.

Giulia Frucci, from the TU/e, for her expertise making measurements with these detectors.

Jeroen Mesman for the development and construction of the insert.

Bert Crama for teaching me about electronic response analysis and for the measurements on the electronic response of our circuit.

Raymond Koehler for the development and the providing of the electronics inside the cryostat, especially the printed circuit board on the sample holder.

Arno van Amersfoort for his advice and construction of the electronic circuit outside the cryostat.

Klara Uhlirova for her assistance and expertise in using the cryostat.

References

[1] K. M. Rosfjord, J. K. W. Yang, E. A. Dauler, A. J. Kerman, V. Anant, B. M. Voronov, G. N. Gol'tsman, K. K. Berggren, 'Nanowire Single-photon detector with an integrated optical cavity and anti-reflection coating', Opt. Express, Vol. 14, Issue 2, pp. 527-534 (2006).

[2] E. A. Dauler, B. S. Robinson, A. J. Kerman, J. K. W. Yang, K. M. Rosfjord, V. Anant, B. Voronov, G. Gol'tsman, K. K. Berggren, 'Multi-element superconducting nanowire single-photon detector', IEEE Transactions on applied superconductivity, vol. 17, no. 2 (2007).

[3] E. Knill, R. Laflamme, G. J. Milburn, 'A scheme for efficient quantum computation with linear optics', Nature 409, 46-52 (2001).

[4] B. S. Robinson, A. J. Kerman, E. A. Dauler, R. J. Barron, D. O. Caplan, M. L. Stevens, J. J. Carney, S. A. Hamilton, '781 Mbit/s photon-counting optical communications using a superconducting nanowire detector', Opt. Lett. 31, 4, p. 444 (2006).

[5] W. J. Skocpol, M. R. Beasley, M. Tinkham, 'Self-heating hotspots in superconducting thin-film microcbridges', J. Appl. Phys. 45, 4054 (1974).

[6] A. G. Kozorezov, A. F. Volkov, J. K. Wigmore, A. Peacock, A. Poelaert, R. den Hartog, 'Quasiparticle-phonon downconversion in nonequilibrium superconductors', Phys. Rev. B, Volume 61, number 17 (2000).

[7] M. Hofherr, D. Rall, K. Ilin, M. Siegel, A. Semenov, H.-W. Hubers, and N. A. Gippius, 'Intrinsic detection efficiency of superconducting nanowire single-photon detectors with different thicknesses,' Journal of Applied Physics 108, 014507 (2010).

[8] A. J. Kerman, E. A. Dauler, W. E. Keicher, J. K. W. Yang, K. K Berggren, G. Gol'tsman, B. Voronov, 'Kinetic-inductance-limitied reset time of superconducting nanowire photon counters', App. Phys. Letters 88, 111116 (2006).

[9] J. E. Mooij, 'Two-dimensional transition in superconducting films and junction arrays', in 'Percolation, Localization, and Superconductivity', edt. A. M. Goldman, S. A. Wolf, Plenum Press, New York, 1984.

[10] L. G. Aslamazov, A. I. Larkin, 'The influence of fluctuation pairing of electrons on the conductivity of normal metal', Phys. Lett. 26A, 238

(1968); Fiz. Tverd. Tela (Leningrad) 10, 1140 (1968); Sov. Phys. Solid State 10, 875 (1968).

[11] J. M. Kosterlitz, D. J. Thouless, 'Ordering, metastability and phase transitions in two-dimensional systems', J. Phys. C 6, 1181 (1973).

[12] S. Eley, S. Gopalakrishnan, P. M. Goldbart, N. Mason, 'Approaching zero-temperature metallic states in mesoscopic superconductor-normal-superconductor arrays', Nat. Phys, 2154 (2011), including 'Supplementary Information: Approaching zero-temperature metallic states in mesoscopic superconductor-normal-superconductor arrays'.

[13] J. Bardeen, 'Critical fields and currents in superconductors', Rev. Mod. Phys. 34, 667 (1962).

[14] A. T. Fiory, A. F. Hebard, W. I. Glaberson, 'Superconducting phase transitions in indium/indium-oxide thin-film composites', Phys. Rev. B 28, 5075 (1983).

[15] M. Tinkham, 'Introduction to superconductivity', Second edition, McGraw-Hill, New York, 1996.

[16] J. W. Ekin, 'Experimental Techniques for Low-Temperature Measurements' Oxford University Press, 2007.

[17] A. Rothwarf, B. Taylor, 'Measurement of recombination lifetimes in superconductors', Phys. Rev. Lett. 19, 27 (1976).

[18] D. Twerenbold, 'Nonequilibrium model of the superconducting tunnel junction x-ray detector', Phys. Rev. B 34, 7748 (1986).

[19] A. Poelaert, A. G. Kozorezov, A. Peacock, J. K. Wigmore, 'Strong nonlinear response of superconducting tunnel junctions due to localized traps', Phys. Rev. Lett. 82, 1257 (1999).

[20] A. G. Kozorezov, J. K. Wigmore, D. Martin, P. Verhoeve, A. Peacock, 'Electron energy down-conversion in thin superconducting films', Phys. Rev. B 75, 094513 (2007).

[21] J. Zhang, W. Slysz, A. Pearlman, A. Verevkin, Roman Sobolewski, O. Okunev, G. Chulkova, G. N. Gol'tsman, 'Time delay of resistive-state formation in superconducting stripes excited by single optical photons', Phys. Rev. B 67, 132508 (2003).

[22] A. J. Kerman, e. A. Dauler, J. K. W. Yang, K. M. Rosfjord, V. Anant, K. K. Berggren, G. Gol'tsman, B. Voronov, 'Constriction-limited detection efficiency of superconducting nanowire single-photon detectors', arXiv:physics/0611260v2 [physics.ins-det], (2007).

[23] A. J. Kerman, J. K. W. Yang, R. J. Molnar, E. A. Dauler, K. K. Berggren, 'Electrothermal feedback in superconducting nanowire single-photon detectors', Phys. Rev. B 79, 100509(R) (2009).

[24] S. Adam, L. Piraux, S. Michotte, D. Lucot, D. Mailly, 'Stabilization of non-self-spreading hotspots in current- and voltage-biased superconducting NbN microstrips', Supercond. Sci. Technol. 22, 105010 (2009).

[25] A. K. Elmurodov, F. M Peeters, D. Y. Vodolazov, S. Michotte, S. Adam, F. de Menten de Horne, L. Piraux, D. Lucot and D. Mailly, 'Phase-slip phenomena in NbN superconducting naowires with leads', Phys. Rev. B 78, 214519 (2008).

[26] J. R. Clem, K. K. Berggren, 'Geometry-dependent critical currents in superconducting nanocircuits', Phys. Rev. B 84, 174510 (2011).

[27] A. Gaggero, S. J. Nejad, F. Marsili, F. Mattioli, R. Leoni, D. Bitauld, D. Sahin, G. J. Hamhuis, R. Noetzel, R. Sanjines, and a. Fiore, 'Nanowire superconducting single-photon detectors on GaAs for integrated quantum photonic applications,' Applied Physics Letters 97, 151108 (2010).

[28] G. Frucci, TU/e, private communication.

[29] Quantum Design, Physical Property Measurement System, Hardware Manual, Part Number 1070, 150B.

[30] http://en.wikipedia.org/wiki/Cupronickel

[31] http://en.wikipedia.org/wiki/Copper

[32] http://en.wikipedia.org/wiki/Gold

[33] http://en.wikipedia.org/wiki/Helium

[34] E. Driessen, 'Coupling light to periodic nanostructures', Casimir PhD Series, Delft-Leiden, 2009-008.

[35] NI DAQPad -6015/6016 Family Specifications, p 7. DAQ E Series, E Series User Manual, 370503K-01, National Instruments Corporation, February 2007.

[36] Model 2000 Multimeter Users Manual, Keithley Instruments, 2000-900-01 Rev. J/August 2010, p. 7 and 2000 61/2-Digit Multimeter, Model 2000 specifications, Keithley Instruments, p. 3.

[37] Agilent 34410A/11A 6 Digit Multimeter, User's Guide, Agilent technologies Fifth Edition. February 2012, p. 125.

[38] Agilent 53131A/132A, 225 MHz Universal Counter, Operating Guide, Agilent Technologies, Manual Part Number 53131-90055, October 2006.

[39] Agilent 53131A/132A, 225 MHz Universal Counters, Programming Guide, Agilent Technologies, Manual Part Number 53131-90044, October 2006.

[40] D. Pöschl, Hirose Electric Europe B.V., private communication.

[41] L.F. Goodrich, S.L. Bray, 'Current ripple effect on superconductive d.c. critical current measurements', Cryogenics 28, issue 11, p. 737-743 (1988).

[42] J. K. W. Yang, A. J. Kerman, E. A. Dauler, V. Anant, K. M. Rosfjord, K. K. Berggren, 'Modeling the electrical and thermal response of superconducting nanowire single-photon detectors', IEEE Transactions on Applied Superconductivity, vol. 17, no. 2 (2007).

[43] F. Mattioli, R. Leoni, A. Gaggero, M. G. Castellano, P. Carelli, F. Marsili, A. Fiore, 'Electrical characterization of superconducting single-photon detectors', Journal of Applied Physics 101, 054302 (2007).

[44] Product name: 'Vacuum Pressure Feedthrough - Fiber Optic', OZ Optics, www.ozoptics.com.